Experimental study on tsunami-driven debris damming loads on columns of an elevated coastal structure

Myung Jin Koh[a], Hyoungsu Park[b*], Jayasekara R. Jayasekara[c], Sabarethinam Kameshwar[d], Kellen Doyle[e], Daniel Cox[f], and Pedro Lomonaco[g]

[a] Graduate Student, Department of Civil, Environmental, and Construction Engineering, University of Hawai'i at Manoa, Honolulu, HI, 96822; email: myungj@hawaii.edu
[b] Assistant Professor, Department of Civil, Environmental, and Construction Engineering, University of Hawai'i at Manoa, Honolulu, HI, 96822; email: hpark9@hawaii.edu *Corresponding Author
[c] Graduate Student, Department of Civil and Environmental Engineering, Louisiana State University, Baton Rouge, LA, 70803; email: jjayas2@lsu.edu
[d] Assistant Professor, Department of Civil and Environmental Engineering, Louisiana State University, Baton Rouge, LA, 70803; email: skameshwar1@lsu.edu
[e] Graduate Student, School of Civil and Construction Engineering, Oregon State University, Corvallis, OR 97331; email: doyleke@oregonstate.edu
[f] Professor, School of Civil and Construction Engineering, Oregon State University, Corvallis, OR 97331; email: dan.cox@oregonstate.edu
[g] Director, O.H. Hinsdale Wave Research Laboratory, College of Engineering, Oregon State University, Corvallis, OR 97331; email: pedro.lomonaco@oregonstate.edu

Abstract

This study presents experimental findings on debris damming loads on columns of an elevated coastal structure under tsunami-like wave conditions. A total of 183 cases (140 with and 43 without debris) were tested at a 1:20 scale to understand the impact of various factors on debris-driven damming loads, including wave characteristics, structure configurations, and debris shapes. The debris impact and damming processes were observed and quantified from optical measurements, and corresponding loads were measured on the entire structure using a force balance plate and on an individual column in the front row using a multi-axial load cell. The experimental results indicated the debris damming load on the entire column structure increased by up to 3.2 times compared to conditions without debris, while the load on the individual column increased by up to 11.0 times. The total damming loads for the whole structure increased, but the load for the individual column decreased at a reduced opening ratio. The smaller debris sizes relative to column spacing showed significantly lower chances of debris damming across different column configurations. Overall, the load on the whole structure showed stronger correlations between debris damming loads and hydro-kinematic variables such as flow depth, velocity, momentum flux, and Froude number compared to the loads on the individual column. Among these variables, momentum flux emerged as the most consistently influential across all categories.

Key words: tsunami, experiment, debris damming, damming loads, column structures

1. Introduction

Extreme overland flows, particularly those triggered by events like tsunamis, cause significant damage in coastal communities. Particularly, the overland flow over a coastal community could transport a substantial amount of water-borne debris inland, including marine vessels, shipping containers, wood utility poles, logs, vehicles, and fragments of damaged or whole structures (e.g., Yeh, 2014; Naito et al., 2014). Typical water-borne debris can worsen damage to the built environment by imposing additional structural loads from impact and damming effects (Reese et al., 2007; Arikawa et al., 2007; Takahashi et al., 2010). The aftermath often includes blocked access and reduced functionality of critical infrastructure systems, especially transportation networks, as seen in the impact of debris accumulation on roads and bridges following such events (e.g., Ghobarah et al., 2006; Kameshwar et al., 2021). Furthermore, debris clearance and removal are vital for community recovery efforts, with associated costs often constituting a substantial portion of total disaster recovery expenses (FEMA, 2007).

In general, tsunami-induced loads on structures can be primarily classified into two types: a) flow-induced and b) debris-driven. Flow-induced hydrostatic and hydrodynamic loads are caused by the direct interaction of the flow with structures and have been the focus of past studies (e.g., Santo and Roberson, 2010; Nouri et al., 2010; Nistor et al., 2011; Chock et al., 2016). Consequently, flow-induced loads have been understood relatively well and adapted to the current design code in the US (ASCE 7, 2016). However, debris-driven loadings are much more complicated and severe. Interactions between flow and debris (e.g., debris entrainment and transport) and consequent debris-structure interaction cause debris-induced loads. Here, a collision between floating debris and structures results in initial impact loading. As the overland flow continues, debris interacts with structures, and debris can block and accumulate in front of a structure and increase flow obstruction, resulting in debris damming loading. At the same time, debris dams also increase upstream water surface elevation and may alter flow fields significantly. This phenomenon potentially obstructs openings and alters hydrostatic and hydrodynamic loads on the structure. For example, the observations from events like the 2011 Tohoku Tsunami suggest that certain mitigation techniques, such as breakaway walls, may be less effective due to transported debris blocking their intended openings (Chock, 2016). Despite a good understanding of flow-induced hydrostatic and hydrodynamic loads, the comprehension of debris-driven loads, particularly damming loads, remains quite limited. However, predicting and quantifying these represent significant challenges due to complex interactions among flow dynamics, debris behavior, and structural configurations (ASCE 7, 2022).

The comprehensive study of debris damming has primarily been limited to the context of river engineering. Bocchiola et al. (2006) analyzed the spatial distribution of debris damming, revealing a correlation between the length of debris and its capture rate, with longer debris more likely to form stable dams through a "bridging" mechanism. Parola (2000) identified critical bridge piers located near the thalweg of a channel due to secondary flows directing debris toward deeper, faster-flowing conditions. Furthermore, Schmocker and Hager (2013) studied the formation of debris dams at debris racks in steady-state flow, elucidating the temporal evolution of the debris dam formation process.

In the wake of the 2011 Tohoku tsunami, several studies have delved into the realm of tsunami debris, utilizing scaled hydraulic experiments. These investigations by Yeom et al., 2009, Nouri et al., 2010, Ko et al., 2015, Riggs et al., 2014, Shafiei et al., 2016, and Stolle et al., 2017 have predominantly focused on assessing the impact loads of debris on structures, employing a relatively simple cuboid or cylinder-shaped debris. Recently, experimental studies, including those by Stolle et al., 2018, Wüthrich et al., 2020, and Shekhar et al., 2020, have sought to investigate debris accumulation behavior under varied debris and building geometry conditions and its effects on structures. To be specific, Stolle et al., 2018 utilized five-column structures as obstacles in the whole channel to measure damming effects on an entire structure and tested with 1:50 scaled cuboid and cylinder-shaped debris. Wüthrich et al., 2020 examined the effect of debris damming on a 1:30 scaled structure due to varied opening conditions. Shekhar et al., 2020 evaluate debris (cuboid shape) impact and damming on an elevated but fully closed structure. Those studies highlighted the need for innovative approaches to reduce experimental uncertainties and inform design guidelines effectively, especially considering the lack of field data complicating experimental design efforts. However, these studies focused on the damming effect on the entire structure, and research simultaneously examining the damming loading on both entire structures and structural elements is exceptionally rare.

This paper focused on introducing newly conducted 1:20 scaled experimental results that analyzed debris damming loads on columns of elevated structures. The study quantified the debris damming process and investigated factors such as debris size, flow conditions, and the number of columns (different openings) on the structure that could characterize debris damming loads on an individual column and the entire structure. The major objectives of this study are to 1) improve the understanding of multi-debris transport, collision, and sequential debris damming on column structures, 2) quantify debris damming loads under varied factors, including debris shape, flow conditions, and structural configurations with varied openings, and 3) evaluate the dominant factors for the debris damming and quantify the correlations of available variables with the damming loads and uncertainties. Section 2 introduces the experimental setup and the test matrix. Section 3 presents preliminary hydrodynamic results on the test setup under clean water (no debris) cases. Section 4 provides the debris damming process and loading characteristics from measured gauges, sensors, and video data. Section 5 evaluates the correlation of flow variables and test conditions to the debris damming loadings. Section 6 discusses the limits of current studies and future work. Section 7 summarizes the general findings and conclusions from this study.

2. Physical Model Setup

2.1 Flume and measurement setup

Experiments of water-borne debris damming on a structure were conducted at the Large Wave Flume (LWF) in Oregon State University's Hinsdale Wave Research Laboratory (HWRL). With adjustable bathymetry, the LWF measured 104 m long, 3.66 m wide, and 4.60 m deep. The LWF was equipped with a piston-type wavemaker that can generate various types of waves, including a solitary wave and transient (tsunami-like) wave, utilizing the full stroke displacement of the wavemaker. This experiment aimed to replicate the depth-limited breaking of incident waves, resulting in a broken tsunami-like bore spreading over a wet bed across the level test section. This setup mimicked tsunami overland flow scenarios over substantial debris sources, such as port container facilities, intending to examine the interaction between such bores and potential debris, as well as other structures, within a controlled experimental setting. However, it is worthy to note here that the applied tsunami-like wave in this experiment has a much shorter period compared to real-world tsunamis and may have a limitation in that the wave energy diminishes before the maximum debris dam is formed.

Fig. 1. displays the profile and plan view of the flume bathymetry and measurement device setup. The flume bathymetry featured a flat offshore section extending 17.68 m from the neutral position of the wavemaker before reaching the first bathymetric concrete slab (at Bay 3) — a horizontal slab measuring 3.64 m in length and rising 0.15 m above the baseline of the flume. The bathymetry consisted of two sloping sections between Bay 4 to Bay 11. The first measured 10.98 m in length with a height of 0.92 m (~1:12 slope) while the second slope measured 14.64 m in length with a height of 0.61 m (~1:24 slope). Beyond the two slopes, the bathymetry transitioned into a flat section from Bay 11 to Bay 18 for the debris platform (gray trapezoid) and the structure (yellow box). The flat section was elevated 1.75 m above the flume's bottom. This elevated flat section measured 25.60 m before leading to a 14.64 m long slope with a height of 0.92 m (1:12 slope), extending to the end of the flume. This is an idealized coastal profile representing urban coastlines and potential debris hazards from shipping containers and vehicles, which are located inland (flat section).

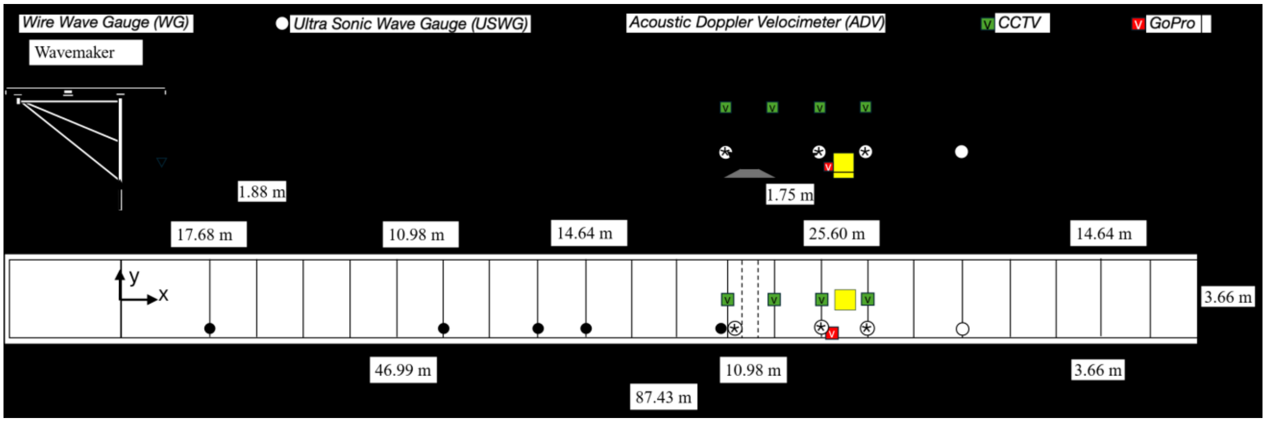

Fig 1. Sketches of the Large wave flume for the experiment: A Profile view (top) and plan view (bottom).

Water surface elevations were measured using five wire-resistance wave gauges (WG) along the flume and four ultrasonic wave gauges (USWG, TS-30S1-IV, Senix, 100 Hz). Three acoustic Doppler velocimeters (ADV, Nortek Vectrino+, Nortek, 100 Hz) were installed with USWGs at the debris platform, as well as at the front and back of the structure. However, ADVs were only used to measure flow velocities in conditions without debris. All three ADVs were removed during the trials with debris to avoid potential collisions and damage during the test. For the optical measurement of debris transport and damming process during the test, the plan view of debris was recorded through four overhanging CCTV (closed-circuit television, Reolink, 25 fps, 4K), and the side view of debris was recorded using an action camera (GoPro, 60 fps, 5K) near the structure. Table 1 provides the location of the center point of each measurement device, including specific x, y, and z coordinates. In this context, the origin of the x and y coordinates indicates the center of the wavemaker, which is in a neutral position, as shown in Fig. 1. Additionally, z = 0 represents the flume bottom elevation.

Table 1. Instrument locations.

Instrument description	Instrument	x (m)	y (m)	z (m)
Wavemaker displacement	WMDISP	-	-	-
Wavemaker wave gage	WMWG	-	-	-
Resistive wave gage	WG 1	10.301	-1.385	-
Resistive wave gage	WG 2	28.591	-1.377	-
Resistive wave gage	WG 3	35.891	-1.377	-
Resistive wave gage	WG 4	39.545	-1.374	-
Resistive wave gage	WG 5	50.484	-1.460	-
Ultrasonic wave gage	USWG 1	50.505	-0.926	3.030
Ultrasonic wave gage	USWG 2	57.787	-1.372	3.334
Ultrasonic wave gage	USWG 3	61.437	-1.363	3.334
Ultrasonic wave gage	USWG 4	68.759	-1.367	3.330
Acoustic Doppler velocimeter	ADV 1	50.486	-1.294	1.769

Acoustic Doppler velocimeter	ADV 2	57.787	-1.636	1.765
Acoustic Doppler velocimeter	ADV 3	61.424	-1.647	1.771
Force Balance Plate	FBP	59.612	-	-
Load cell	LC	59.505	-0.013	1.769
Closed-circuit television	CAM 1	50.695	-0.059	5.289
Closed-circuit television	CAM 2	54.299	0.018	5.223
Closed-circuit television	CAM 3	57.944	-0.040	5.208
Closed-circuit television	CAM 4	61.624	-0.006	5.220
Handheld Digital Camera	GoPro	59.070	-1.688	2.797

2.2 Test structure setup

The 1:20 length scale for this study was designed considering an elevated coastal structure focusing on the potential debris damming exerted on the columns. The test structure was installed on the centerline ($y = 0$) of the flat section measuring 1.219 m long and 1.219 m wide, including the cover plate, and consisted of nine aluminum tubing (0.051 m outside width) columns in a 3 x 3 arrangement with 0.458 m between each column's center to others as a default configuration. Each column had a height of 0.65 m, and this fixed height was sufficient to avoid overtopping of columns during the experiment. In our test, a superstructure above the column was not considered to ensure clear visibility for measuring the debris damming process on the structure.

Fig. 2a shows a detailed 3-D view of the test structure. Two types of measurement devices were installed below the cover plate to measure time-varying loading on the test structure. First, the Force Balance Plate (FBP, AF 32-12-K, Advanced Mechanical Technology Inc, 1,000 Hz) was located at the very bottom of the test structure. The FBP is a box-shaped device that consists of four tri-axial load cells mounted on a stiff frame at each corner to measure the total loading on the structure. Second, a pancake-shaped single multi-axial load cell (LC, Omega191 SI 7200-1400, ATI, 100 Hz) was installed under the column in the middle of the front row to measure the loading at the single column (Fig. 2a). The FBP is a single instrument mounted on a reaction frame, and the LC is attached to the FBP by means of an interface aluminum plate. The whole force measuring system is laid underneath the bed level, minimizing its interference with the flow. This setup allowed for the measurement of the 3-dimensional forces and moments exerted on the whole column structure and the targeted single column separately. To prevent potential bottom profile changes and unnecessary turbulence effects from the ground, an aluminum cover plate, 121.9 cm by 121.9 cm, covered the whole bottom surface of the column structure, and both FBP and LC were completely buried under this cover plate. The surface of the structure cover plate met the same elevation as the ground level ($z = 1.750$ m).

Detailed dimensions and plan views of the three configurations are provided in Fig. 2b, 2c, and 2d. A 3 x 3 arrangement of columns was utilized as a default setup, providing the largest opening width (40.7 cm) between two columns perpendicular to the tsunami waves. To study various opening conditions in the experiment, the column arrangement was adjusted to 3 x 5 and 3 x 7 by adding additional rows of columns, resulting in 17.8 cm and 10.17 cm spacing, respectively. Each configuration, 3 x 3, 3 x 5, and 3 x 7, had a frontal closure ratio of 15.8%, 26.4%, and 36.9%. The frontal closure ratio is defined as the ratio of the projected area of columns in the first row to the overall frontal area of the structure, measured from the outline of the columns, i.e., 96.7 cm.

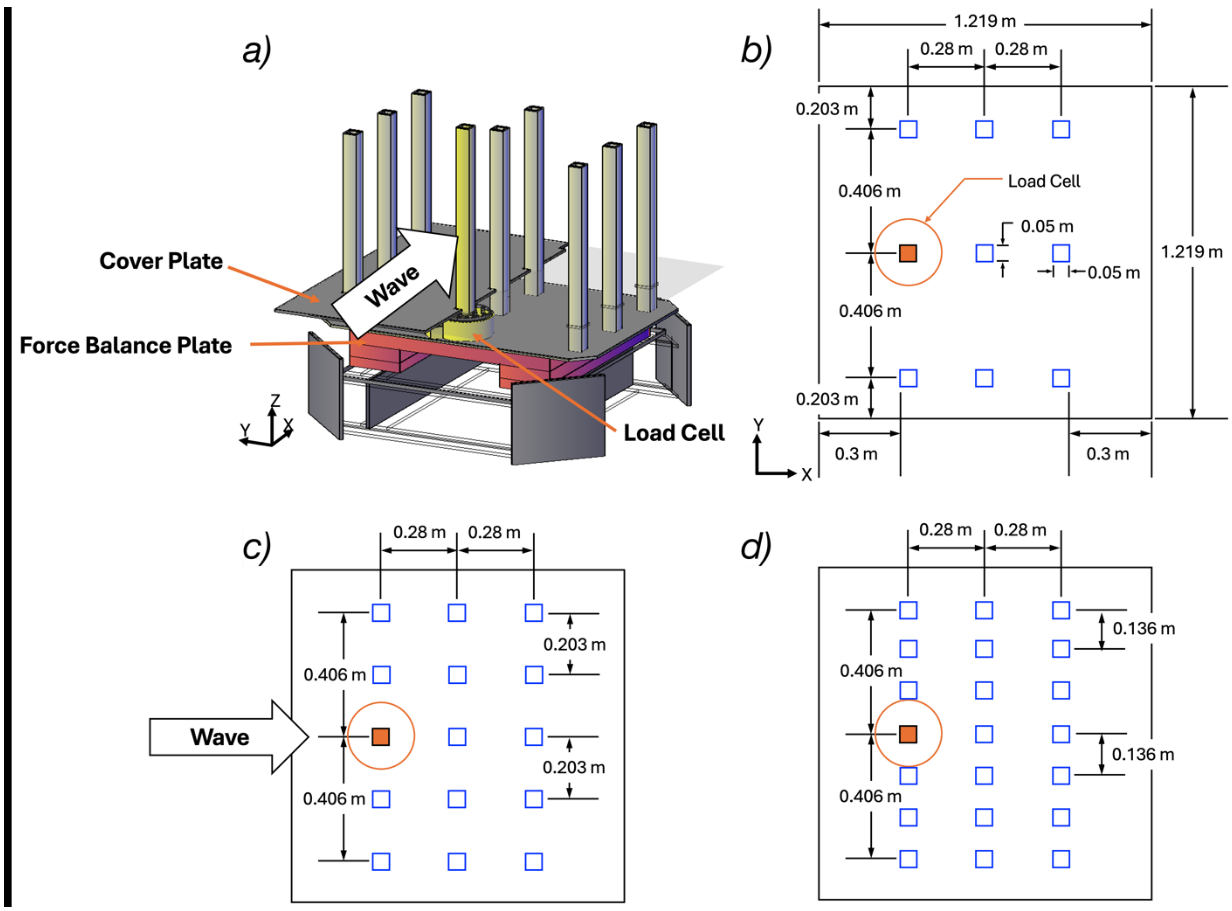

Fig 2. Sketch of the test structure with detailed dimensions. a) 3-D view of the structure, including the Force Balance Plate and Load cell. b) Configuration 1, 3 x 3 columns, c) Configuration 2, 3 x 5 columns, and d) Configuration 3, 3 x 7 columns.

2.3 Debris setup and debris platform

A total of 2 different wooden debris shapes, fabricated at a 1:20 length scale was utilized in this experiment. The debris shape represented an idealized 6.1 m (20 ft) shipping container, and a 12.2 m (40 ft) shipping container (Fig 3). The scaled debris measured: a) 6.1 m shipping container, 29.80 cm long, 11.43 cm wide, and 11.43 cm high; b) 12.2 m shipping container, 59.60 cm long, 11.43 cm wide, and 11.43

cm high. The debris was coated with water-resistant paint to minimize potential damage and density changes and to increase visibility during the test. The measured mean density of two types of painted debris was 544 kg/m^3. Here, it is worth noting that the exact density and length (width and height) of shipping containers were not scaled. The weights and centroid of actual shipping containers vary, but a uniform weight for debris was used for simplicity. Therefore, the current debris setup may exceed the maximum weight capacity of shipping containers. After several preliminary tests underwater, the debris was reweighted, and less than a ±2% change in the density compared to the original mean density was observed.

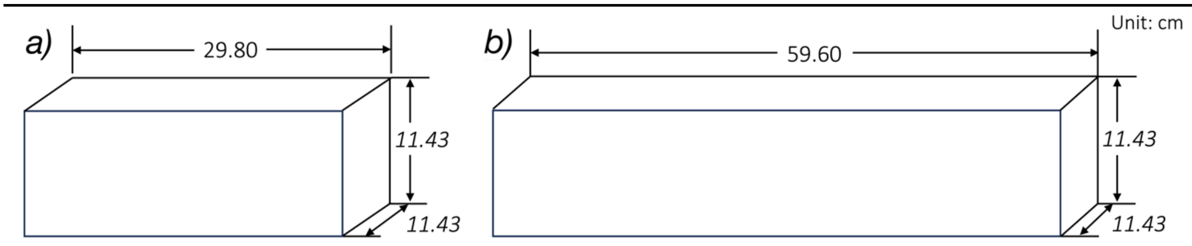

Fig 3. Sketch and dimensions of debris in cm: a) 6.1 m shipping container, and b) 12.2 m shipping container.

The debris entrainment (incipient motion) process and the repeatability of the test are sensitive to the initial position of debris and the bottom friction on the ground. It was observed that high friction (e.g., with concrete) on the ground may cause unnecessary damage to debris during repeated tests (Park et al., 2021). To minimize uncertainties related to ground friction, a debris platform, framed with wood and covered with polyvinyl chloride (PVC) plate, was installed (Fig. 4). The debris platform is a symmetrical trapezoid installed between Bay 12 and 13 on the flat section covering the entire width of the flume, starting at x = 50.65 m (Fig. 4a). The platform dimensions were 3.66 m long, 3.66 m wide, and 0.130 m high, with 1:9.4 slopes at the front and back. The elevation of the middle flat section at the debris platform was z = 1.885 m, allowing debris to be located 0.5 cm above the still water depth, z = 1.880 m (Fig. 4b). It's noteworthy that the flat ground elevation at the structure was set as z = 1.750 m, as shown in Fig. 1. The net water depth was 0.130 m above the flat ground elevation of the structure. Once the leading edge of the tsunami-like wave reaches the debris platform, the entrained debris by water moves toward the platform and floats without much dragging due to this initial water depth above the flat ground. Moreover, this initial water depth maintains debris floating during the whole wave propagation so that any bottom friction effects on the damming process can be excluded, except at the initial dragging during entrainment.

In addition, tests were also conducted with the PVC cover plate case, which involved installing only the PVC cover plate without the trapezoidal wood frame (Fig. 4c and d). In this case, the elevation of the middle flat section at the PVC cover was z = 1.763 m, allowing debris to be located about 1.7 cm under the still water depth, z = 1.780 m. More details will be provided in Section 2.4 Wave condition and test matrix.

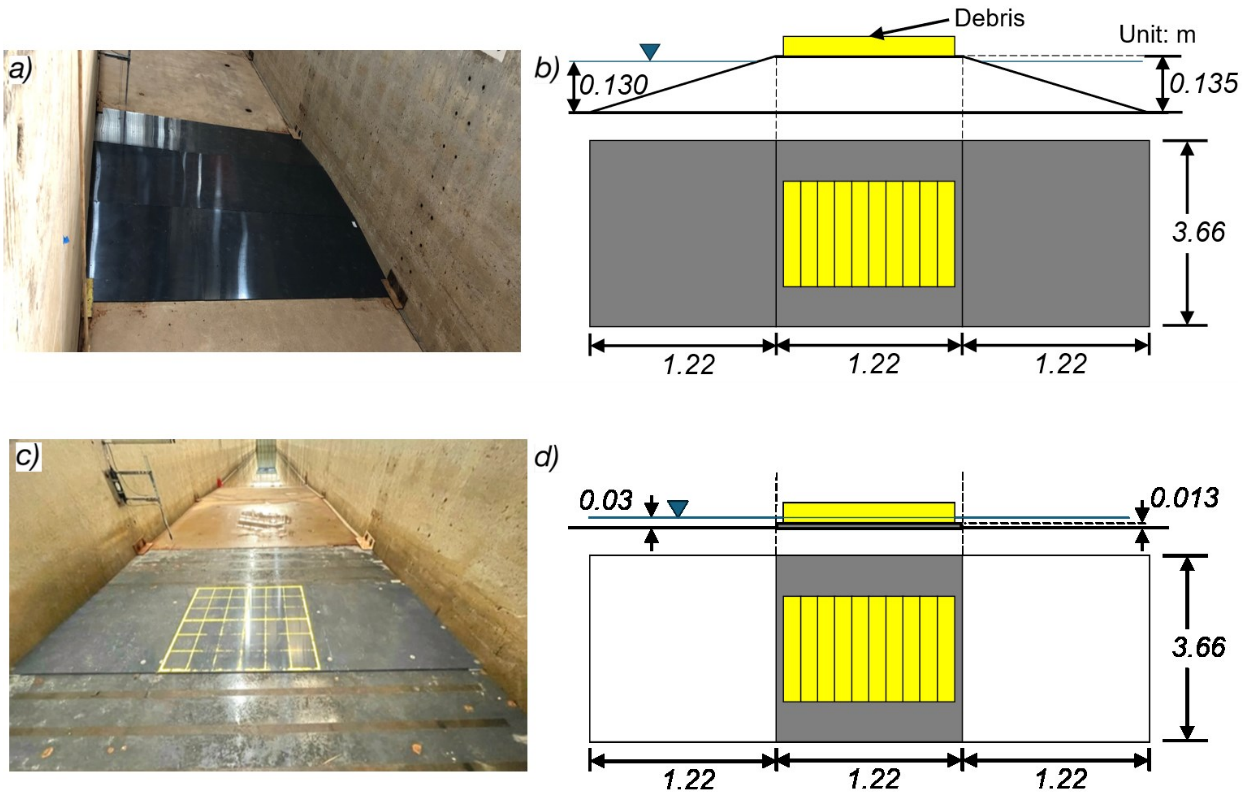

Fig. 4. a) Picture of the debris platform, b) from top to bottom: side and top views of the platform, c) picture of the PVC cover plate, and d) side and top views of the plate and sample debris (12.2 m shipping containers) at the beginning of each trial.

The distance from the debris platform to the structure was set as 6.71 m (center of the debris platform to the front of the column structure) after the preliminary test before installing the structure. For consistency of initial debris positioning during the experiment, yellow grid lines were painted at the center of the flat area on the debris platform. The grid line area measures 1.20 m by 1.20 m squares with a spacing of 0.20 m. During the preliminary test, various initial placements and amounts of debris were tested to determine the optimal initial position of debris for maximizing debris damming at the structure. After numerous trials, we determined the initial position and number of debris units for each debris shape that maximizes debris damming on the structure. Fig. 5 illustrates each selected initial debris placement developed for the damming test of each debris group: a) fifteen 6.1 m shipping containers, and b) ten 12.2 m containers. `

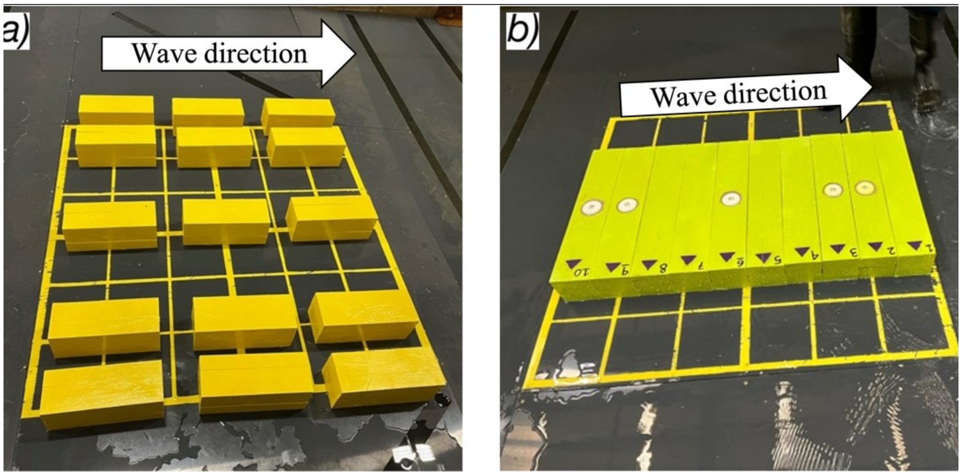

Fig. 5. Initial configuration of a) 6.1 m shipping container, and b) 12.2 m shipping container.

The static friction coefficient (μ_s) was measured to quantify friction of debris to the debris platform under dry and slightly wet conditions using $\mu_s = tan\theta$, where θ is the slope of a plate that is impending a slide. Debris was placed on a PVC plate, and then the slope of the plate was increased until the debris started to slide down. Average $\mu_s$equal to 0.328 and 0.320 were observed for dry and slightly wet conditions, respectively, and the tests were repeated five times each for averaging values. Also, by using $\mu_k = tan\theta - \frac{a}{gcos\theta}$, the kinetic friction coefficient (μ_k) was also obtained as 0.271 for dry and 0.204 for wet condition where a is the acceleration of debris measured by a Xsens DOT IMU sensor (www.xsens.com) and g is the gravitational acceleration. The Xsens DOT accelerometer (Alaka et al., 2023; Shultz, J., 2022) has a compact size (< 3.6 cm in length), waterproof design, and lightweight (~10 g). Fig. 5b shows the white cap on some debris elements designed to place the IMU inside.

2.4 Wave conditions and test matrix

A total of six tsunami-like (transient) waves were utilized in our experiment. The 4 m full-stroke of the piston-type wavemaker in the LWF was utilized to give a maximum flow duration. The speed of each full stroke of the wavemaker was determined by paddle displacement data, as shown in Fig. 6. As the paddle speed increases, the consequential wave has a shorter length but a more significant wave height in general. This transient wave condition was utilized in previous physical modeling studies for tsunamis (e.g., Park et al., 2013; Ko et al., 2015; Park et al., 2021). During a preliminary test with debris, more than ten different paddle displacement time series were tested, and three representative wave conditions were selected. All three wave conditions showed flow depths sufficient to exceed the maximum draft of each piece of debris and flow speed was high enough to transport all debris from the platform to the structure, allowing a debris dam to form at the structure without significant dragging along the bottom.

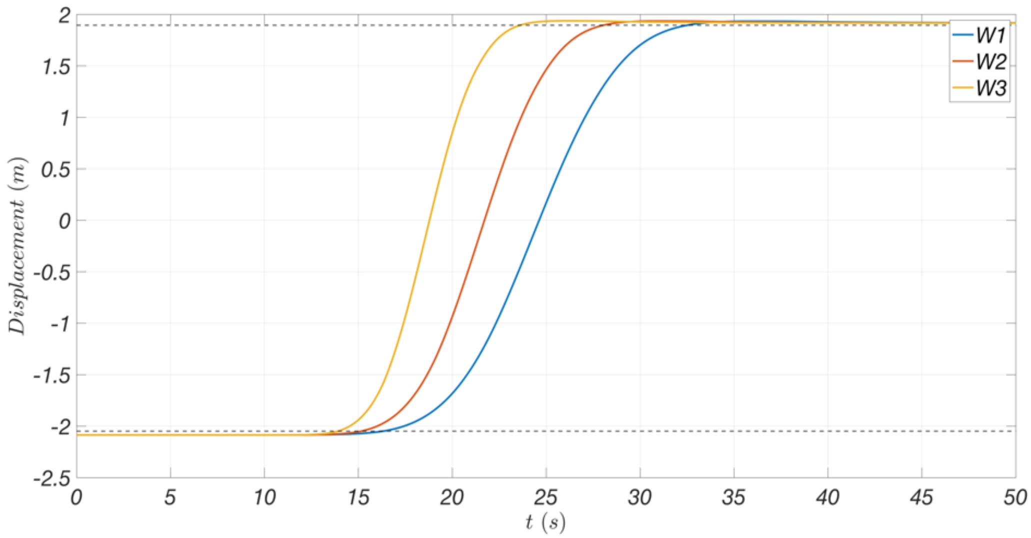

Fig 6. Three selected wavemaker paddle displacement time series to generate W1 (blue), W2 (orange), and W3 (yellow) tsunami-like wave conditions.

While three wavemaker displacement inputs were utilized for waves, two different still-water depth conditions were adopted: 1) h = 1.880 m for "with debris platform case" and 2) h = 1.780 m for "with PVC cover plate case." Therefore, a total of six wave conditions were tested. Initially, three paddle displacement functions (W1, W2, and W3) were selected and tested with the debris platform (shown in Fig. 4 and 5) as a default test setup. To distinguish the other three sets with "PVC cover plate case," we refer to the default wave conditions as W1A, W2A, and W3A. Subsequently, another three sets of waves refer to W1B, W2B, and W3B, which utilized the same paddle displacement functions as W1, W2, and W3, while lowering water depth and removing the debris platform except a PVC cover plate, which has 1.2 cm thickness. In the PVC cover plate case, debris couldn't be secured without lowering the water depth due to a higher initial water depth (13 cm) than the draft of debris. To keep posing debris at the same position and minimize potential dragging during the damming process, the still water depth was decreased to h = 1.780 m, resulting in a 3.0 cm initial water depth above the ground at the structure. So, debris is partially submerged about 1.8 cm (3.0 cm – 1.2 cm), while it is secured by its weight.

Table 2 provides a summary of the selected wave properties characterized by wavemaker displacement time, T_{WMDISP}, still water depth at the flume bottom, h, still water depth at the structure, d_0, the maximum free surface elevation, η_{max} at WG1 (near the wavemaker at Bay 1), and the maximum flow depth above the ground, d_{max} at USWG 2 (near the structure at Bay 14). The wavemaker displacement time (T_{WMDISP}) was defined as the effective displaced time of the paddle between 99% of minimum and maximum locations (dashed lines in Fig. 6). The range of T_{WMDISP} are 16.19 s for W1, 12.97 s for W2, and 9.80 s for W3, respectively. An increase in η_{max} and d_{max} for shorter T_{WMDISP} was observed as the increase of paddle velocities in general. In the case of the wave with the PVC cover plate, because of lowered h, slightly lower d_{max} was observed.

Table 2. Experimental wave conditions.

Debris Platform Type	Wave Type	T_{WMDISP} (s)	h (m)	d_0 (m)	η_{max} (m)	d_{max} (m)
					WG 1	USWG 2
Debris Platform (A)	W1A	16.19	1.88	0.13	0.325	0.318
	W2A	12.97	1.88	0.13	0.371	0.352
	W3A	9.80	1.88	0.13	0.454	0.399
PVC cover plate (B)	W1B	16.19	1.78	0.03	0.225	0.211
	W2B	12.97	1.78	0.03	0.269	0.232
	W3B	9.80	1.78	0.03	0.349	0.277

In this experimental study, a total of 183 tests, including 43 tests without debris, were conducted based on the combination of debris platforms, waves, configurations of the structure, and debris shape to understand the effect of these variables on debris-driven damming loadings on the structure. Table 3 shows the summary of test conditions and the number of repeats. Here, Conf. 2 in W1B, W2B, and W3B is marked with an asterisk because those total 27 cases were excluded from this analysis due to unclear patterns in the Force Balance Plate. In the end, 156 trials were selected and analyzed herein.

Table 3. Combination of experimental cases and number of repeats

Debris Platform Type (DPT)	Wave Type	Configuration (Columns)	Debris type		
			non-debris	Homogeneous	
			Hydro	D1	D2
Debris Platform (A)	W1A	Conf. 1 (3 x 3)	4	3	7
		Conf. 2 (3 x 5)	3	6	6
		Conf. 3 (3 x 7)	1	6	3
	W2A	Conf. 1 (3 x 3)	4	3	8
		Conf. 2 (3 x 5)	3	6	6
		Conf. 3 (3 x 7)	1	11	8
	W3A	Conf. 1 (3 x 3)	4	3	6
		Conf. 2 (3 x 5)	3	6	5
		Conf. 3 (3 x 7)	1	6	3
PVC cover plate (B)	W1B	Conf. 1 (3 x 3)	3	3	4
		*Conf. 2 (3 x 5)	4	3	2
	W2B	Conf. 1 (3 x 3)	3	3	4
		*Conf. 2 (3 x 5)	3	3	3
	W3B	Conf. 1 (3 x 3)	3	3	4
		*Conf. 2 (3 x 5)	3	3	3
Total	183		43	68	72

Asterisk marks show the excluded trials due to unclear pattern in loading data.

3. Hydrodynamic analysis (non-debris conditions)

3.1 Characteristics of hydro kinematics

The hydro kinematics are fundamental variables to understand debris damming on structures and corresponding loading conditions. The Hydro (non-debris) case in Table 3 was utilized to understand the hydro kinematics, including the surface elevation and flow velocity at the debris platform and near the structure, and to understand the time-dependent hydraulic loadings without debris on the structure. All measured hydro kinematics data from wave gauges and ADVs were synchronized with the load cell, Force Balance Plate data, and recorded video to quantify the accurate relation between wave and loading conditions. The initial bore arrival time at the seaward side of the columns was used as a reference to synchronize the recorded video with the corresponding data time series. Here, the synchronization between videos and DAQ data was performed utilizing the LED ramp that was connected to DAQ and recorded by videos. The initial bore arrival time at the seaward side of the columns was used as a reference to synchronize the recorded video with the corresponding data time series. The data acquisition system (DAQ) and FBP recorded data for 200 seconds, with sampling rates of 100 Hz for the DAQ and 1,000 Hz for the FBP, respectively. Fig. 7 shows the time series of a sample trial with a W2A wave and Conf. 3 (3 x 7) structure without introducing any debris (non-debris case). Fig.7a shows free surface elevations (η) obtained from WG 1~3 and USWG 1~3. It shows that the free surface profile shoaled over the slope and broke before reaching the structure. The maximum elevation is measured at WG 3 (η_{max}= 0.28 m). Peak velocity of the flow in the x-direction yields 1.44 m/s at ADV 1, 1.15 m/s at ADV 2, and 1.52 at ADV 3. (Fig. 7b). The measured results show that free surface elevation at offshore (USWG2) was higher than the rear of the structure (USWG3). In contrast, velocity increased when passing the structure.

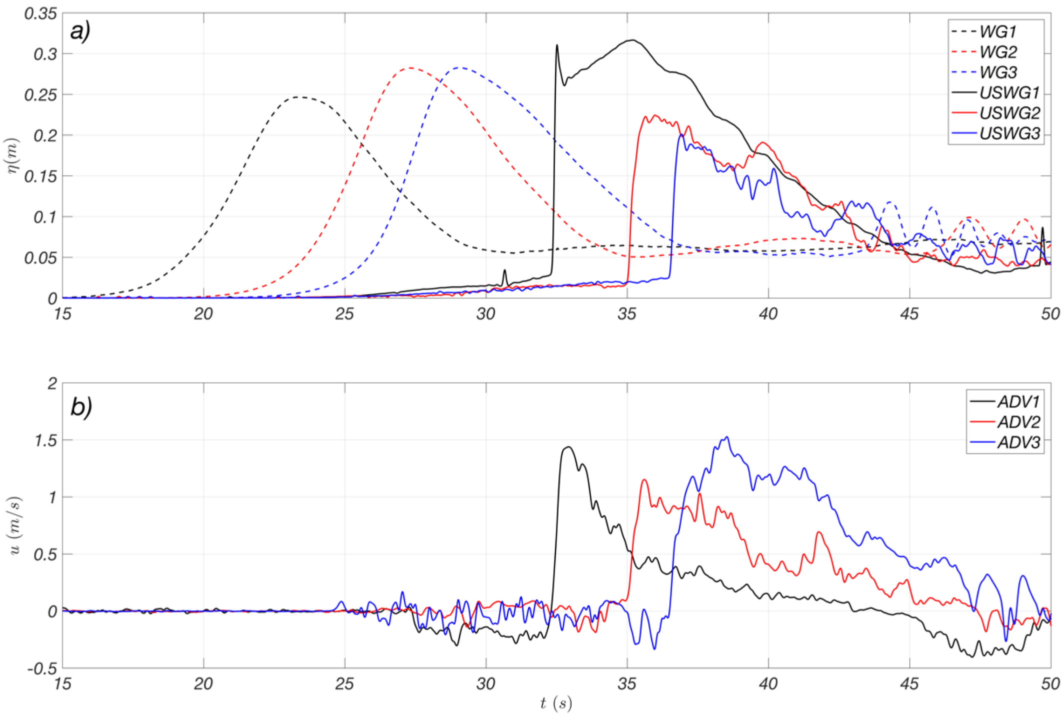

Fig. 7. Time series of (a) surface elevation at wave gauges and (b) x-velocities for non-debris conditions at W2A and Conf.3.

In the current physical model setup, no instruments were installed at the structure to avoid disruptions in video recording. To get kinematic data at the structure (frontal column position, x = 59.49 m), data obtained from the two pairs of measuring instruments (USWG 2, 3 and ADV 2, 3) that were installed in front (x= 57.79 m) and behind (x = 61.44 m) of the structure, was interpolated. Fig. 8 shows the time series for W2A obtained from USWGs, ADVs, and interpolated data according to the relative distance from the sample position to the structure. Fig 8a shows the flow depth, d at USWG 2 (red dash-dot), USWG 3 (blue dash-dot), and the structure (black solid) for the W2A wave condition. Here, flow depth, $d = \eta + d_0$, is the net flow surface elevation. Additionally, d_0 is the still water depth at the structure above the ground, so $d_0 = 13$ cm for the case with the debris platform. Fig. 8b displays the velocity along the x-direction, u, at ADV 2 and 3 (red and blue dash-dot) and the structure (black solid). Those interpolated kinematic data provided averaged values between two measured points, and Figs. 8c and 8d show the calculated momentum flux ($M = du^2$) and Froude number ($Fr = u/\sqrt{gd}$) calculated by using the interpolated d and u.

As the tsunami-like wave inputs utilized the full stroke of wavemaker displacement, both flow depth and x-velocity eventually decreased once they reached their peak, albeit at slightly different phases. Specifically, Fig. 8a and 8b illustrate the overall decrease of both flow depth and velocity. Flow depth maintained relatively constant values between 36 and 38 seconds, while the velocity remained relatively constant between 37 and 39 seconds. The corresponding momentum flux showed a clear peak at 37 seconds and displayed much sharper decreases thereafter.

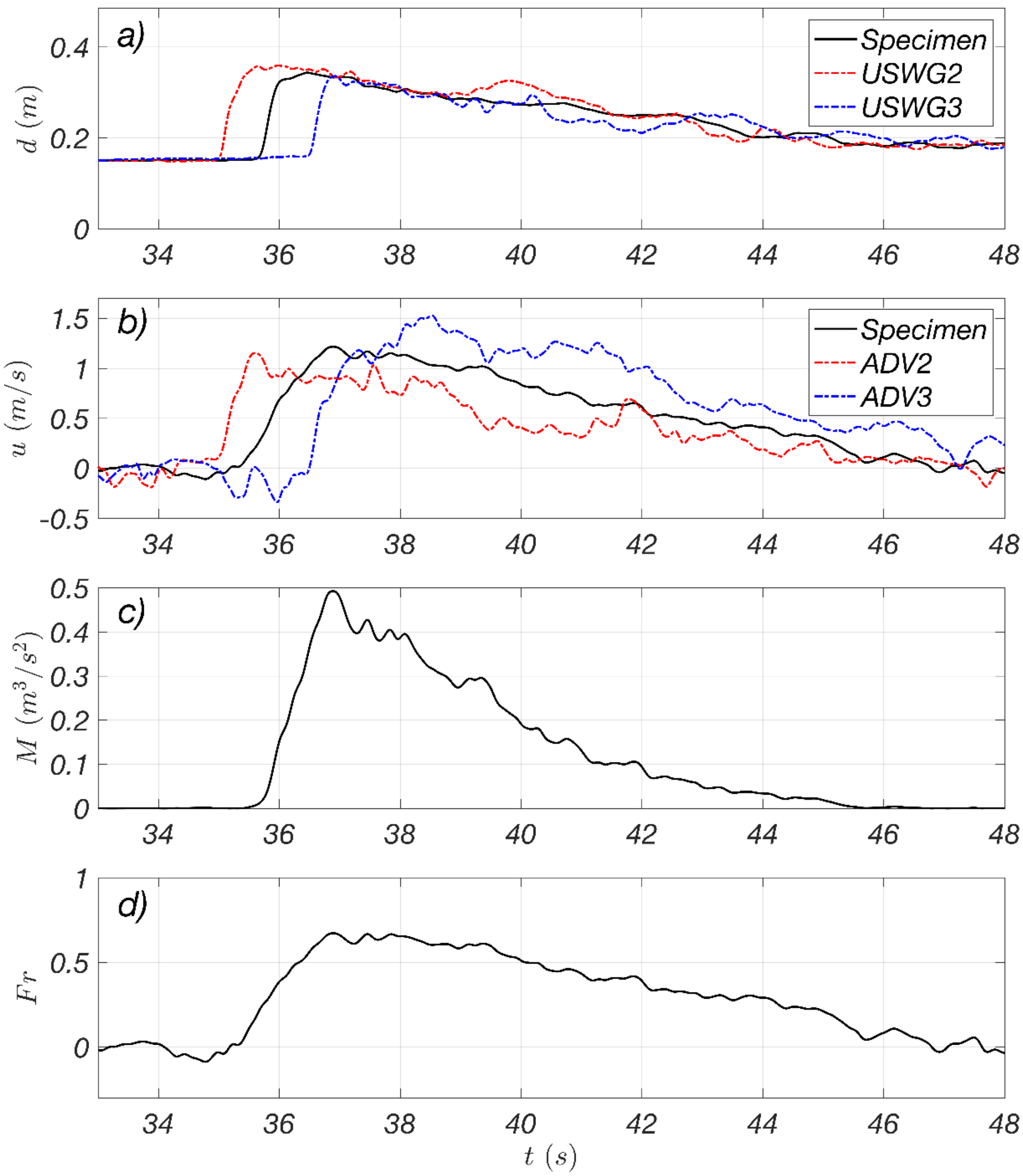

Fig 8. Sample time series of ensemble average of transient wave kinematics for W2A wave at the front of the structure (x=59.49 m): a) flow depth, b) *x*-velocity, c) momentum flux, and d) Froude number; red dash-dot, blue dash-dot, and black solid lines indicate the data obtained at USWG 2 and ADV 2(in front of the structure), USWG 3 and ADV 3 (behind the structure), and interpolated at the structure, respectively.

Overall, the fluctuation in flow kinematics is more substantial compared to realistic tsunami waves, which are defined by pseudo-steady flow conditions. Therefore, the measured debris damming loads in our test are also influenced by the timing of when the debris damming occurs. However, the Froude number, a dimensionless parameter used to characterize flow conditions, showed relatively mild variations between

36 and 42 seconds. As will be shown later, most debris damming occurred during this time frame. Specifically, Froude numbers were mostly stationary between 36.5 and 40.0 seconds, and the ranges were approximately 0.5 to 0.6, while the range of momentum fluxes was between 0.2 ~ 0.5 m^3/s^2, respectively.

Based on the measurements from Fig. 8, Table 4 lists the maximum values of the interpolated d, u, M, Fr, $\overline{Fr}$, and σ (standard deviation of Fr). Here, $\overline{Fr}$ is the timely averaged Froude number over the specific time ranges when the momentum flux exceeded 20% of its maximum value ($M > 0.2 \times M_{max}$). Here, we chose 20% for the effective time span during which the most significant debris damming was observed in most trials. This time span corresponds to 36 seconds to 42 seconds for W2A as shown in Fig. 8c and only used to estimate $\overline{Fr}$. In general, d_{max}, u_{max}, and M_{max} show increasing values from W1A to W3A for debris platform cases, and from W1B to W3B, for PVC cover plate cases. The maximum and averaged Froude numbers from the experiments have ranged from 0.676 to 0.985 and from 0.515 to 0.729, respectively.

Table 4. Hydrodynamic characteristics at the structure (non-debris case)

Wave Type	d_{max} (m)	u_{max} (m/s)	M_{max} (m^3/s^2)	Fr_{min}	Fr_{max}	$\overline{Fr}$	σ
W1A	0.310	1.135	0.367	0.096	0.683	0.515	0.116
W2A	0.338	1.216	0.497	0.112	0.676	0.542	0.114
W3A	0.385	1.637	0.982	0.159	0.882	0.646	0.124
W1B	0.203	0.983	0.190	0.130	0.738	0.594	0.097
W2B	0.225	1.134	0.284	0.175	0.815	0.610	0.099
W3B	0.254	1.532	0.594	0.223	0.985	0.729	0.125

3.2 Characteristics of hydrodynamic loadings (non-debris case)

The forces exerted on the whole structure were measured through the Force Balance Plate (FBP), and the forces exerted on the front column from the Load Cell (LC) were measured in non–debris cases. Fig.9 shows the *x*-direction force (F_x), *y*-direction force (F_y), and horizontal force, $F_h = \sqrt{F_x^2 + F_y^2}$ exerted on both the structure and the middle column during W2A and W2B. The trials for W2A-Conf. 1, W2A-Conf. 2, W2A-Conf. 3, and W2B-Conf. 1 were repeated more than three times each. Each black, blue, and red line shows the ensemble-averaged time series of each case, W2A-Conf. 1, 2, and 3, respectively, and the yellow line shows W2B-Conf. 1. Here, the light gray line shows repeated single trials in each case.

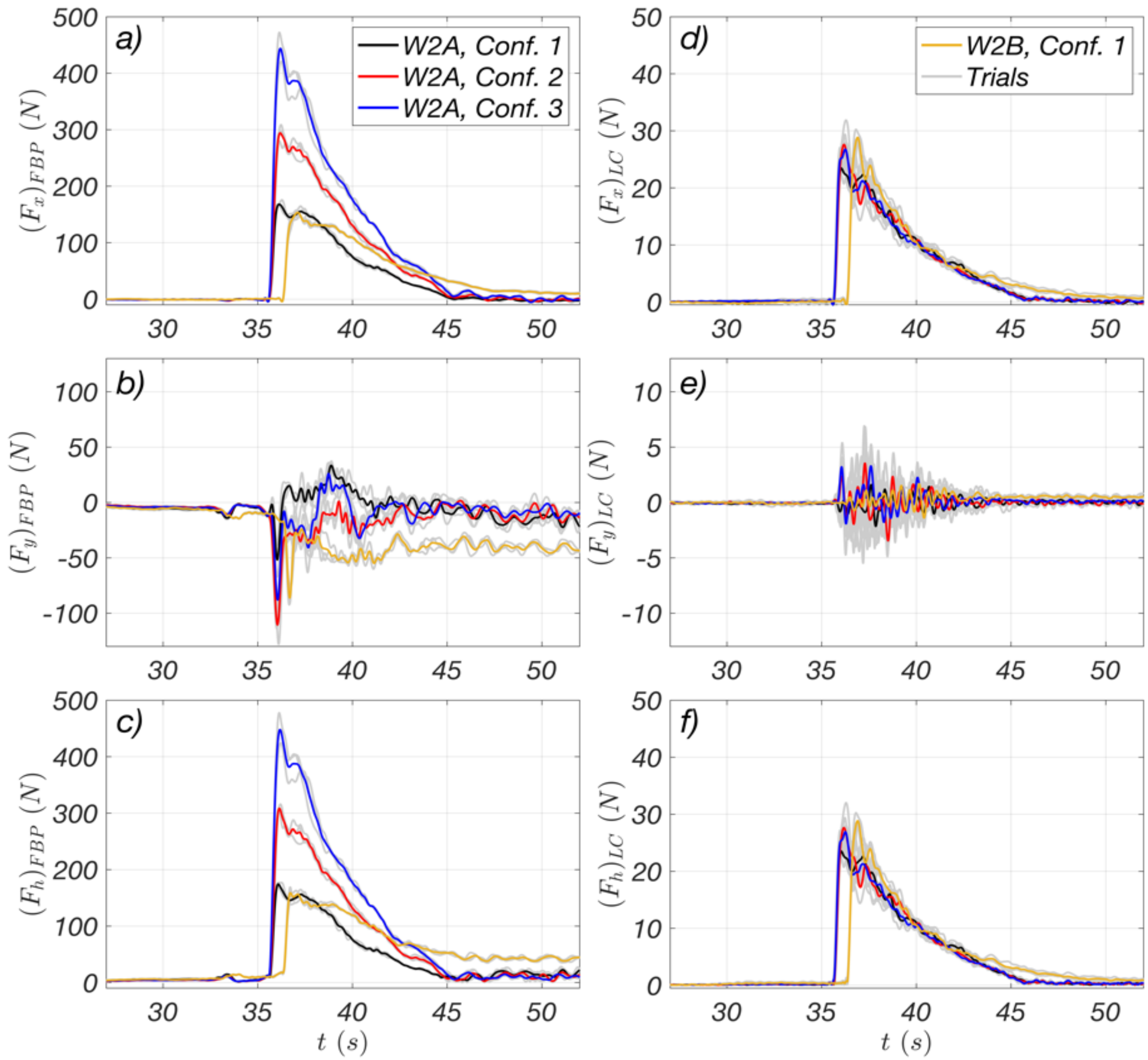

Fig. 9. Time series of x, y, and total horizontal forces at the structure, FBP, (a, b, and c) and the middle column, LC (d, e, and f). Each black, red, blue, and yellow line shows the ensemble-averaged time series of each case, and the light gray line shows repeated single trials in each case.

In the case of x-directional force at the structure, $(F_x)_{FBP}$, the largest force was measured for Conf. 3 (3 x 7 columns), and the smallest force was measured for Conf. 1 (3 x 3 columns), as seen in Fig. 9a. As expected, forces increase in the flow direction as the projected area of the structure increases with additional columns at the structure. Here, we can measure a similar time series of force between W2A-Conf. 1 (black) and W2B-Conf. 1 (yellow) as they utilized the same wavemaker paddle function. However, the force from W2B-Conf. 1 was measured with a delay of about 0.8 s because of a relatively smaller flow depth, as observed in Table 2.

Both results of F_y on the structure (Fig. 9b) and the middle column (Fig. 9e) showed slightly asymmetric forces, but the magnitudes of F_x are larger than F_y, and the moment of peak forces are mostly dominated by flow directional force. Thus, the horizontal force, F_h, showed a very similar maximum peak value and pattern to that of F_x (Fig. 9c and 9f). All other wave conditions were evaluated for non-debris cases, and the maximum horizontal forces for the structure and the middle column were examined and summarized in Table. 5. Results show that the largest forces were found for W3A or W3B in each configuration, as expected due to the wave height. As we observed in Fig. 9, there was a significant increase in the maximum force at the structure, $\langle F_{FBP} \rangle_{max}$, for all other wave conditions as the number of columns increased from Conf. 1 to Conf. 3. While the maximum force at the loadcell, $\langle F_{LC} \rangle_{max}$ showed relatively minor differences across among different configurations and the smallest force is found at Conf. 1.

Table 5. Maximum horizontal forces, F_h exerted on the single column (F_{LC}) and the structure (F_{FBP})

Wave & DPT	$\langle F_{FBP} \rangle_{max}$ (N)			$\langle F_{LC} \rangle_{max}$ (N)		
	Conf. 1	Conf. 2	Conf. 3	Conf. 1	Conf. 2	Conf. 3
W1A	124.4	215.5	301.0	20.5	23.1	24.0
W2A	175.7	308.8	472.3	25.9	31.9	29.4
W3A	245.6	469.0	667.5	45.5	47.7	48.6
W1B	123.6	-	-	22.9	-	-
W2B	157.8	-	-	30.2	-	-
W3B	212.7	-	-	46.3	-	-

4. Debris loadings results

Debris damming loading is greatly affected by the temporal variation of flow dynamics, leading to complex changes in the behavior of debris damming and sequential loadings over time. Thus, to provide a thorough interpretation of debris damming loading phenomena, it is important to carefully examine the interactions among waves, debris, and structural elements across temporal scales. In this section, a synchronized analysis for damming loadings incorporating recorded video footage and time series data of hydrokinetic parameters, such as surface elevation, velocity, momentum flux, and Froude number, were utilized alongside the corresponding debris damming loading exerted on the whole structure and at its central column.

4.1 Frequency filtering for impact and damming loads

Fig. 10 shows a series of snapshots of the sample trial of the experiment for the W2A - Conf. 1 - D2 case (Fig. 10a through 10h) and a recorded time series of raw data for the structure and the middle column (Fig. 10i) for the same trial. D2 indicates that this trial tested with 10 of 12.2 meters shipping containers. Each snapshot from Fig. 10a to Fig. 10h shows the process of debris transport and development of debris dam on the structure, including initial placement of debris, wave-debris interaction represented as debris entrainment and debris transportation, and wave-debris-structure interaction such as wave impact, debris impact, and debris damming. Specifically, Fig. 10b through 10d show that the incident wave passes over the debris platform, and a bore-type wave is developed while flowing across the debris platform, initiating the transportation of debris. The leading edge of flow reaches the structure at 35.77 s before debris and results in pure-hydrodynamic loads first (Fig. 10e). Then, transported debris collides with the structure at 38.61 s and yields the impact and damming loads (Fig.10f). Also, the additional impact loads were also observed (Fig. 10g and 10h) sequentially. The experiment recorded a certain amount of default noise for the whole time series for the FBP, thus noise removal was conducted, and Fig. 10 showed the results after the noise filtering.

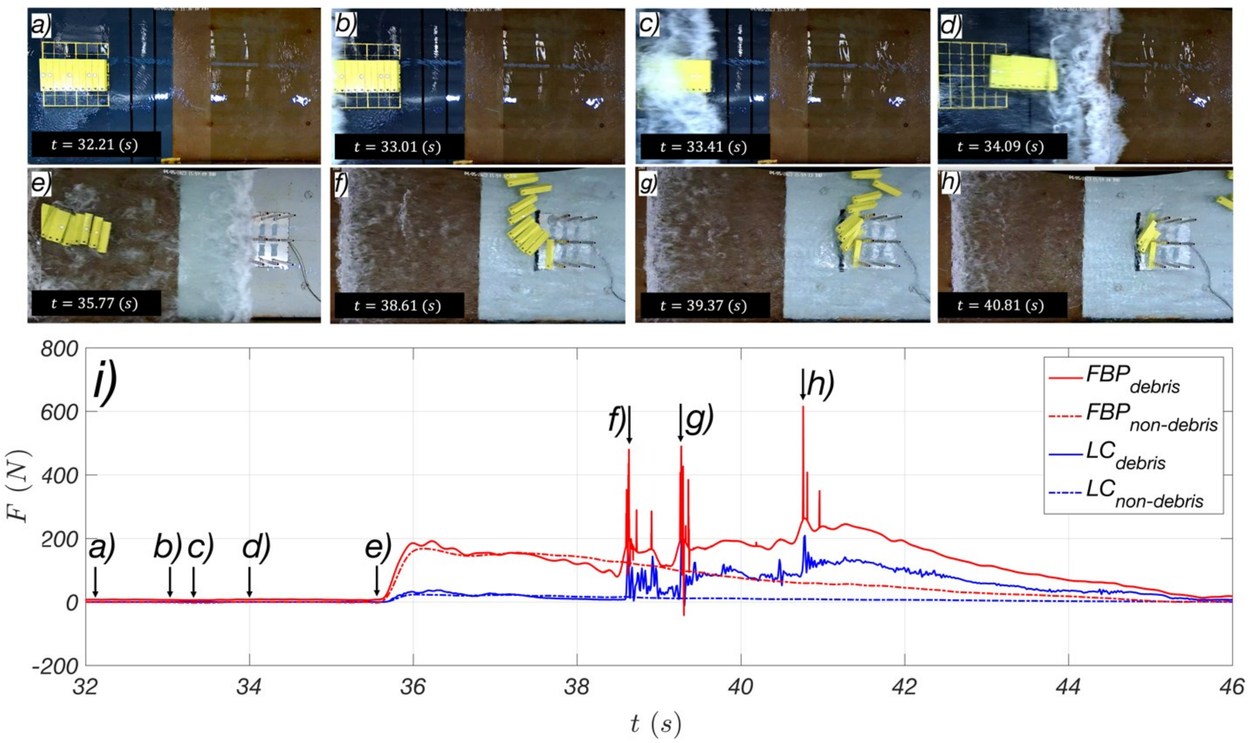

Fig. 10. Snapshots of debris transport and damming process for the W2A-Conf.1-D2 case in a) through b), and i) time series of horizontal force data of with debris case (solid) and without debris case (dash-dot) at the structure (red) and the middle column (blue).

In this study, the water-borne debris load on the structure was considered to have two major loading components. The first is debris impact load, where the debris momentum (because of the collision) is rapidly transferred to the structure. Therefore, the time series of impact load has a very high frequency and short duration. The second is the hydrodynamic load, which corresponds to the inertia and drag forces on the structure because of the changes in flow. When debris collision exits, both the pure hydrodynamic load and the debris damming load are observed before and after the collision of debris on the structure as parts of the overall hydrodynamic load. A larger accumulation of debris at the structure increases the cross-sectional area, which in turn increases the hydraulic drag (hydrodynamic) loads on the structure. Therefore, the damming process is essential for quantifying the debris damming load by separating the force-time histories into impact phases.

For this isolating process, original signals were converted into frequency-domain by fast Fourier transform (FFT), and two filters were applied to the converted signal: A low-pass filter and a high-pass filter following the previous work from Shekhar et al. (2020). The low-pass filter was designed to eliminate frequencies above a predefined limit. For debris damming load, frequencies above 5.0 Hz were completely removed, with a transition zone between 2.5 and 5.0 Hz following the previous work. As a result, frequencies less than 2.5 Hz from the raw force signal are fully visible for the damming load (hydrodynamic loadings). In contrast to the low-pass filter, the high-pass filter was applied to completely filter out frequencies below 2.5 Hz with the same transition zone for impact load. Once the filtering process has been completed, inverse FFT converts the filtered frequency signals back into the time domain.

Fig. 11 displays the total loads (black line), impact loads (red line), damming loads (blue line), and pure-hydrodynamic loads (yellow line) measured at the FBP. As the leading flow arrived at the structure at t = 35.70 s, the pure-hydrodynamic loads were observed before the effective debris collision would occur at t = 38.50 s. Once debris interacts with the structure, we could observe the major impact loads and fluctuations of damming loads from t = 38.5 s to t = 44.0 s due to multiple collisions of debris to the structure during these time spans. The maximum total load at the structure was found at t = 40.76 s with 706.9 N, where the maximum impact load was also observed at the same timestamp with 456.0 N (red asterisk). Here, the maximum damming load (blue asterisk) was found at t = 40.80 s with 238.0 N, almost the same time stamp as the maximum impact load, although the timestamp of each maximum impact and damming loads were found to be different in other trials.

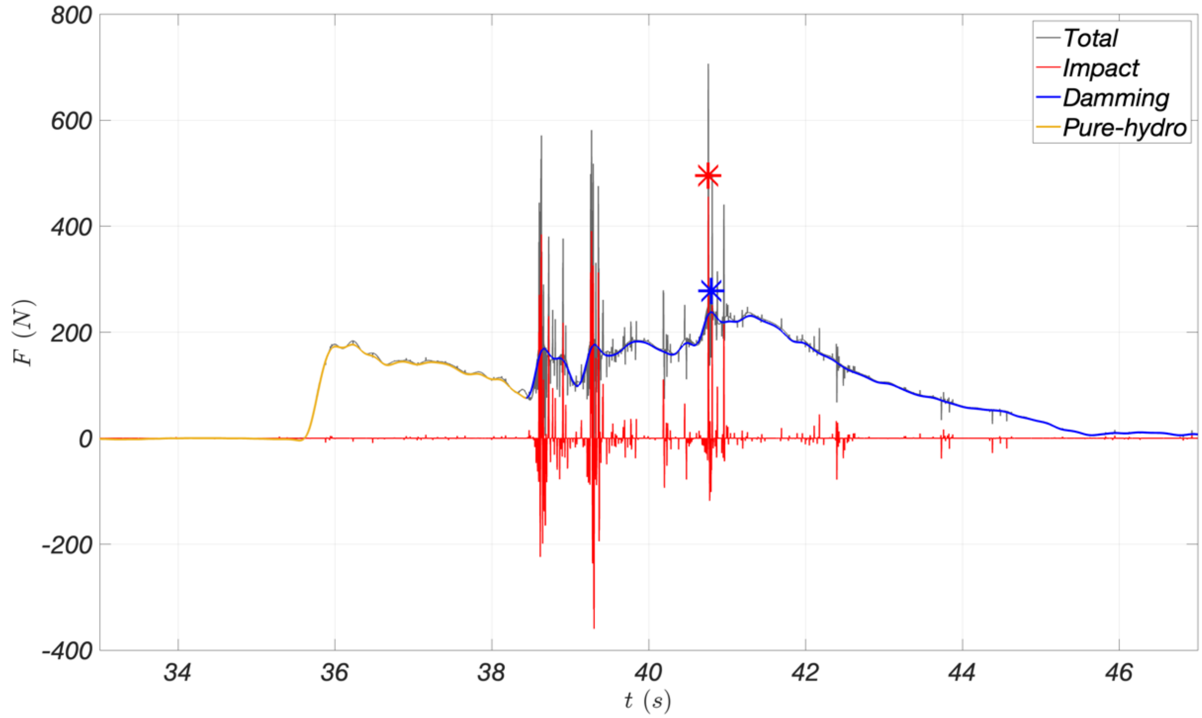

Fig 11. Sample application of low and high pass filter to the FBP measured data at the structure. Each black, red, blue, and yellow line shows the total, impact, damming, and pure-hydrodynamic loads. Here, each red and blue asterisk indicates the maximum impact and damming loads.

In a similar manner, Fig. 12 shows three loads from the LC after the frequency filtering process at the same trial. Similar to the FBP results, the pure-hydrodynamic loads were observed before the effective debris collision occurred at t = 38.50 s. The maximum total load of 275.7 N occurred at *t* = 39.28 s, and the peak impact loading was 178.5 N (red asterisk) at the same time stamp as the maximum total load. However, the maximum damming loads of 130.4 N were observed at *t* = 40.83 s (blue asterisk) about 2.3 s later. This example showed the clearly different time stamps of each peak load for impact and damming loads at the central column. We observed the peak damming load occurred slightly after the impact load at *t* = 40.80 s. This example showed the clearly different time stamps of each peak load for impact and damming loads at the central column. We observed the peak damming load occurred slightly after the impact load at *t* = 40.80 s. However, this impact load is neither maximum impact nor total load.

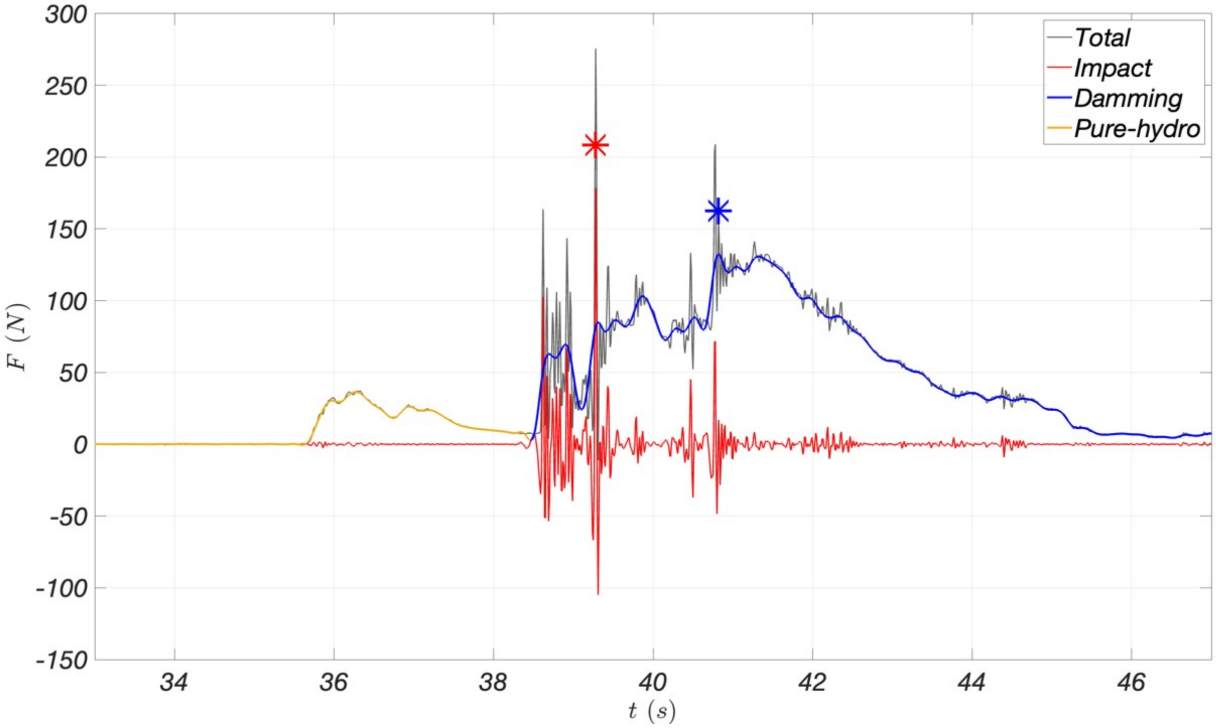

Fig 12. Sample application of low and high pass filter to the LC measurements at the middle column: Each black, red, and blue line shows total load, impact load, and damming load. Here, each red and blue asterisk indicates the maximum impact and damming loads.

In most trials, before and after the maximum impact and damming loads, a series of peak impact or damming loads were also observed. Generally, the maximum peak impact loads occurred earlier than the maximum peak damming loads, but some cases showed only impact loads without debris damming loads when debris didn't effectively create the debris dam at the front.

The time series of impact and damming loads generally showed different characteristics between the total structure (from the FBP) and the frontal middle column (from the LC). Besides, the magnitude and timestamp of each peak, the number of peak damming loads, and the number of impact loadings were also different for each trial. Furthermore, these patterns are inconsistent even for the exact same wave, debris shape and configuration conditions as the debris motions are highly dependent on the complicated flows (turbulences) over the platform and some randomness on the flow and debris interactions at the initial debris entrainment.

Fig. 13 illustrates the maximum impact loads on the structure, as measured by the FBP (Fig. 13a) and the impact loading on the middle column, as measured by the LC (Fig. 13b) in a normalized time domain, ($t^* = (t_{Imp} - t_0)/\sqrt{g/d_{max}}$). Here, t_{Imp} is the time of peak impact loads at each trial and t_0 is the time of leading-edge flow that exceeded 1% of the d_{max}. In this figure, each marker indicates different configurations of the structure such as circle for Conf. 1, square for Conf. 2, and diamond for Conf. 3. Also, the wave and platform conditions are defined by colors such as black, red, and blue with debris platform (A), and purple, orange, and green with PVC plate cover (B) for three waves, W1, W2, and W3, respectively. The hollow and filled symbols indicate two different debris shapes, D1 (6.1 meters containers) and D2 (12.2 meters containers), respectively. Dashed line in color presents a timestamp of leading-edge flow arrival to the structure for each wave and platform condition.

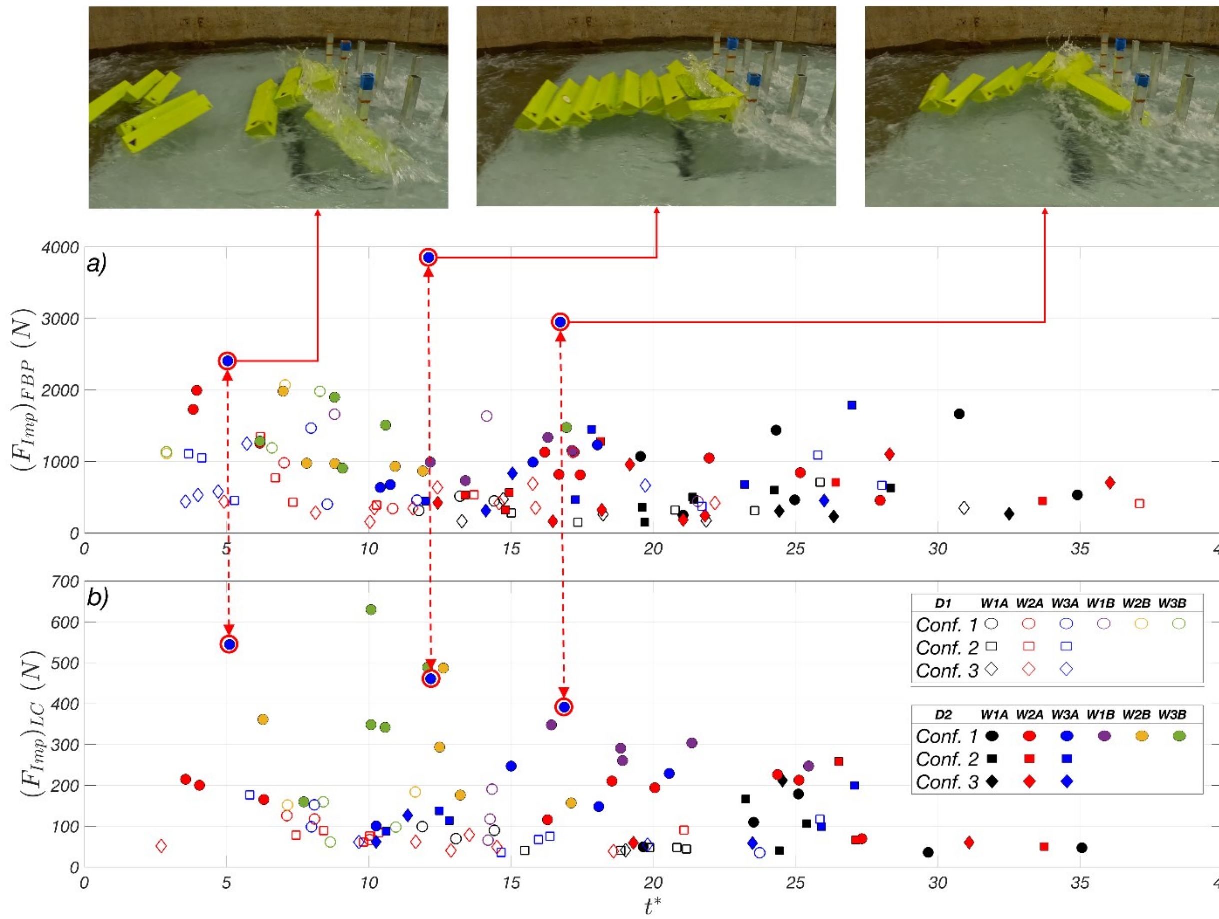

Fig 13. Impact loads on the structure (a) and the middle column (b) and in a normalized time, t^* for the different wave conditions, platform scenarios and debris shapes. The upper panel figure shows a sample snapshot at that time of maximum impact loading for trial for W3A-Conf.1-D2.

Within the impact loads on the structure (Fig. 13a), it was observed that higher impact load typically occurred at D2 (larger debris) and W3, but the magnitude of these impact loadings is also governed by the number of impacting debris and configuration types. Specifically, within the W3A wave conditions for D2 (blue circle with arrows) depicted in Fig. 13a, one can observe the three highest impact loads, which are about 2,405 N, 3,854 N, and 2,950 N, respectively. Among the three, as shown in the upper panel, the largest impact load occurred with 10 debris at t^*=12, and the ratio is shown up to 15.7 times of the maximum load of the non-debris case. The second and third impact load occurred with 7 debris elements and 5 debris elements at t^*=17, and 5, respectively. Additionally, the relatively larger impact loads, including the three highest impact loadings, were all observed in Conf. 1 and much smaller loading in Conf. 3. This may be caused by the stronger backflow intensity at the frontal columns as they have a smaller opening ratio for Conf. 3. As the leading-edge flow reaches to the structure earlier than the debris, the reflected flow in a subcritical flow condition (Fr < 1) could reduce the collision speed of the debris.

In the case of loads at the middle column (Fig. 13b), the maximum impact load was also measured at Conf. 1, which aligns with the impact load at the structure. Specifically, the maximum impact load, i.e., 544 N, was observed to be about 13 times higher than the non-debris case, which showed the third largest impact load at the structure. This discrepancy on the maximum impact loads between the whole structure and the middle column is attributed to the debris predominantly impacting the middle column, thereby concentrating the loads onto a single column, while in other cases, impact loads were distributed across multiple columns.

Overall, the time of the peak impact loads for W1 (black and purple symbols) ranging from $12 < t^* < 35$ for both the structure and the middle column and are slower than those of the other waves. The peak impact loads for W2 and W3 are ranged from $3 < t^* < 37$ and there are no clear patterns on the timestamp of impact loads depending on configurations or debris type.

4.2 Characteristics of debris damming loads

For a better understanding of the debris-driven damming loading mechanism, the time varying changes in damming loads and corresponding flow kinematics were evaluated. However, measuring the time varying changes in flow fields due to debris and structure interactions directly from the measured data was challenging. For example, velocity readings were not available in this experimental setup at the structure due to potential debris collisions with the sensor that may cause damage. Additionally, installing too many wave sensors would have obstructed camera views and hindered tracking of debris motion near the structure. Therefore, herein, the hydro-kinematic data measured in Section 3 (non-debris case) without debris as flow conditions during debris damming was used, assuming that hydrodynamics on non-debris cases are very similar to the one with debris and they are still crucial factors in defining the timely debris damming process. The high pass filtered time series loading data and recorded videos were synchronized with the time series of non-debris data (flow depth, velocity, etc.) in Fig. 14.

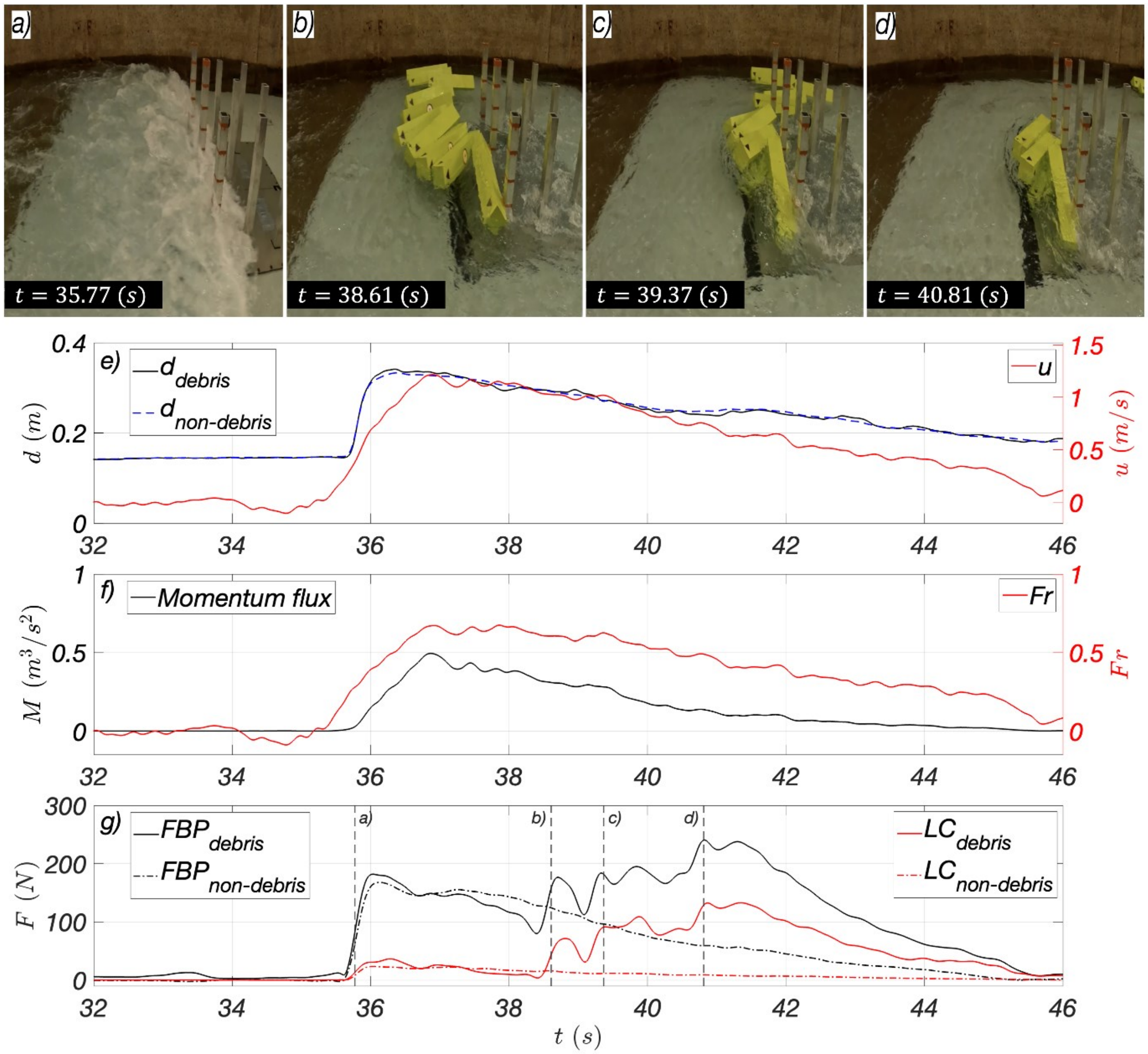

Fig 14. Synchronizing data with recorded video, 12.2 m shipping container: a) leading edge arrives at the structure, b) the first damming peak, c) the second peak, and d) the maximum peak damming loads at the structure, and time series of d with and without debris, u, ηu^2, Fr, and forces measured by FBP and LC in e) through g).

The upper panel of Fig. 14 shows four representative timestamps that are marked for notable changes in the debris damming loads history at the structure, such as the time of leading-edge arrival (Fig. 14a), near the first peak debris damming (Fig. 14b), the second peak debris damming (Fig. 14c), and the maximum peak debris damming (Fig. 14d). The lower panel shows the time series of flow depth, d, x-directional velocity, u, x-directional momentum flux, du^2, Froude number, Fr, for the non-debris cases for reference, and the time series of horizontal loading data of debris damming in the structure (F_{FBP}) and the middle column (F_{LC}) after each filtering. Particularly, Fig. 14e compares the ensemble averaged flow depth in conditions with debris (solid black) and without debris (dashed blue), showing almost identical flow depth profiles. Here, flow depths were measured near the wall (uswg1 and uswg2) of the flume. This indicates that the overall hydro kinematics with and without debris would be very similar in the flume and there are no blockage issues (e.g., Stolle et al., 2018; Wüthrich et al., 2020) under our test condition. However, we could observe local changes on flow depth and velocity at debris damming process through videos near the structure.

From b) to d) the overall damming loads at the time of debris dam formation (or deformation of debris dams) result in varied peak points while time series of damming loads on the structure will generally decrease as flow depth, velocity and momentum flux decrease in our test conditions. However, the maximum damming load was observed at point d). From the timestamp c) to d), the transient motion of debris at the front was settled down and eventually increased the debris damming loads as a more secure debris dam was stabilized.

Besides this sample trial shown in Fig. 14, complicated fluctuations in the time series of damming load from different trials under varied conditions of debris, wave, and configuration were observed. To characterize debris damming loads, three largest peaks damming loads were selected from each trial as representative. Through the observation, we decided to utilize only three peak points per each trial among multiple peak points avoiding too many overlaps, while representing various debris dams at a single trial. Fig. 15 illustrates a sample of our peak detection methodology for damming loads from the same sample case utilized in Fig 14. The figure displays the time series of damming loads, F_{dam} (blue solid line), hydrodynamic loading at the no-debris case, F_0 (black dash-dot line), and the differences between these two loads, F_{net} (red solid line), which is $F_{dam} - F_0$. As observed in Section 3, the hydrodynamic loads on the structure in non-debris case decreased after the initial peak at t = 36.1 s in this figure. To quantify the net debris-driven damming loads on the structure, the time stamps of three points were extracted corresponding to the times of the largest differences in loads to effectively characterize damming loads (reverse triangle) from the time series values of F_{net}. Once, we found three-time stamps, the peak damming loads were read from F_{dam} (blue line) at those three-time stamps. In a similar manner, three peak damming loads were also extracted from the center column by utilizing the LC data.

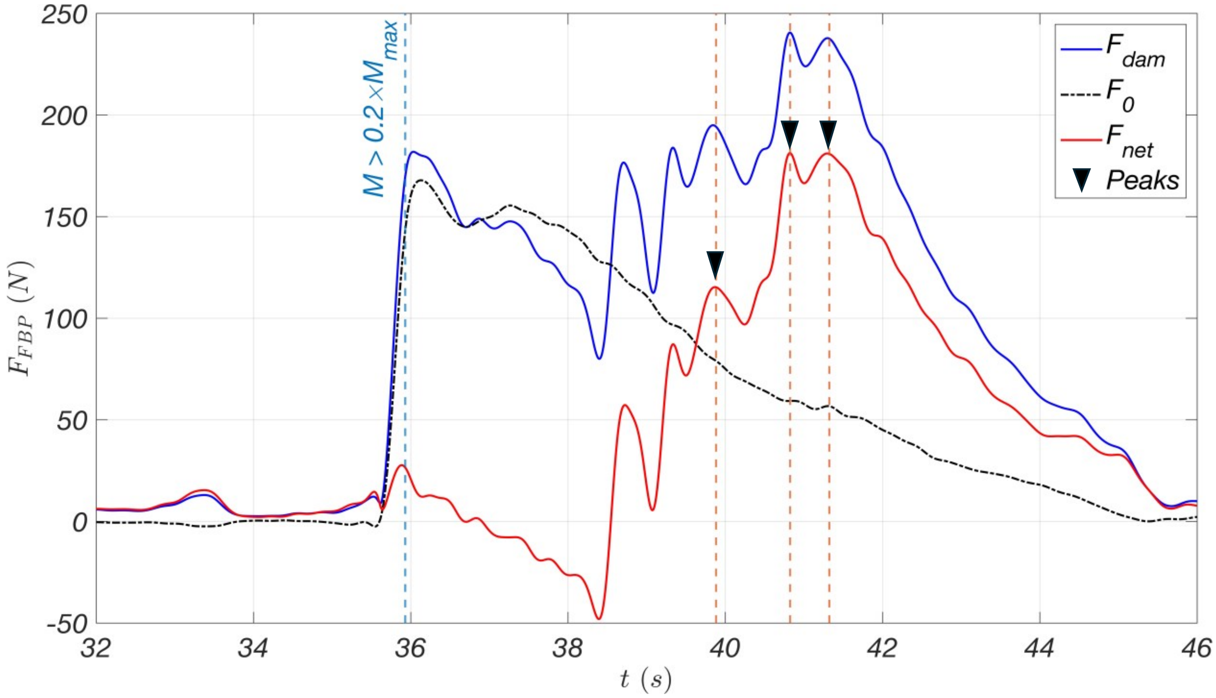

Fig 15. Example of local peak detection on the structure. Measured time series of hydrodynamics (F_0) and total loads on the structure (F_{dam}), as well as net damming loads (F_{net}) with the identification of the three peak time stamps (Peaks).

Following the peak detection methodology, Fig. 16 shows the measured peak damming loads and time on the structure and middle column for all trials. Fig. 16 utilized the exact same format as Fig. 13. Each circle, square, and diamond shape indicates Conf. 1, Conf. 2, and Conf. 3. Also, the wave and platform conditions are defined as colors, and dashed lines in color present timestamp of leading-edge flow. The hollow and filled symbols indicate two different debris shapes, D1 and D2, respectively.

Peak values on the structure (Fig. 16a) show that there was a distinct relationship between waves and damming loads, with the highest load occurring at W3 and the lowest at W1. Furthermore, D2 (filled symbol) consistently exhibited larger loads compared to D1 (void symbol), with observed differences of the maximum damming loads up to approximately 40%. The largest damming loads on the structure was observed in Conf. 3 and the value is about 710 N. In addition, it is worth noting that the overall damming loads during Conf. 3 are larger than Conf. 1 and 2 for all flow conditions. This pattern is expected considering the smaller opening in Conf. 3, which causes relatively more debris damming.

However, the maximum peak damming loads at the middle column (measured with the LC) was observed during Conf. 1 (Fig. 16b) and this value was 311 N. Here, Conf. 1 exhibited much higher loading compared to Conf. 2 and 3, attributed to the concentration of damming over the middle column in Conf. 1, as opposed to the distribution of damming across more columns in Conf. 2 and 3. However, regarding debris size, the damming loads of D1 in Conf. 1 (void circle) was significantly lower or not measured due to the larger spacing between columns relative to the size of the debris, rendering the formation of debris damming more challenging.

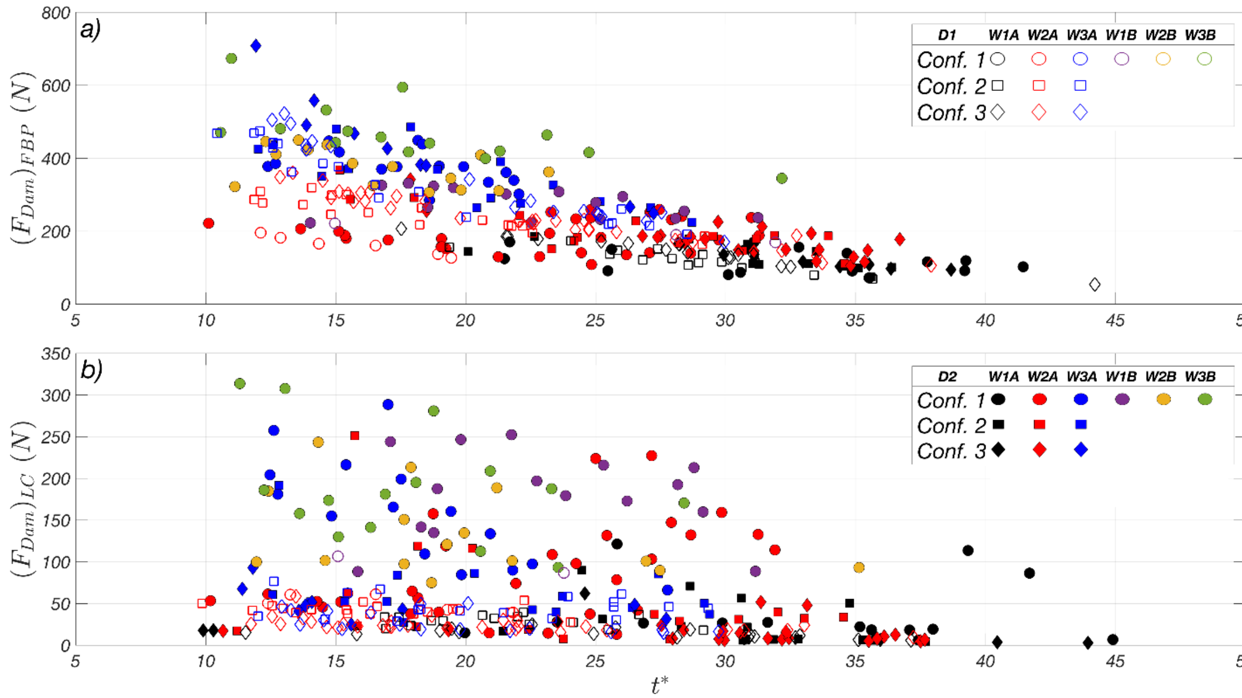

Fig 16. Peak damming loads for all trials on the whole structure (a) and the middle column (b) in a normalized time, t^* for the different wave conditions, platform scenarios and debris shapes.

Similarly, it was observed that the wider spacing of Conf. 1 resulted in less frequent damming occurrences at the front of the structure, and subsequently limited availability of damming data. This was further highlighted when focusing on the D1 case, where the distance between columns measures 40.7 cm for Conf. 1, which is wider than the 29.80 cm length of D1. In a total of eighteen trials of Conf. 1 with D1, only 17% (three trials) displayed effective debris damming, compared to seventeen out of eighteen trials (91%) in Conf. 2 and twenty-three out of twenty-three (100%) in Conf. 3. In contrast, D2, with a length of 59.60 cm, longer than the column spacing in Conf.1, the occurrence of damming on the structure was insensitive to column spacing and showed a consistent probability of damming formation in every configuration, such as thirty-five out of forty (88%) for Conf. 1, fifteen out of seventeen (88%) for Conf. 2, and twelve out of fourteen (86%) for Conf. 3.

Compared with impact loads, the quantity and pattern of debris damming loads were different between the whole structure and middle (single) column. The maximum damming loading was 3.4 times lower than the observed maximum impact loading at the whole column structure and 1.8 times lower than that observed at the single column. The larger damming loads were observed for Conf. 1, while the larger impact loading was observed for Conf. 3 on the structure. However, the larger damming and impact loadings were generally observed for Conf. 1 rather than Conf. 2 and 3 on the middle column. In addition, the earliest timestamp of the peak damming load is t^* = 10, and the maximum damming loads are measured around t^* = 12 for both the structure and the middle column, after which the overall damming loads decrease. This pattern is also observed in the impact loads in Fig. 13, as the flow kinematics (e.g., flow depth, velocity) are overall decreased over time in our test conditions. However, no clear patterns were observed in the timestamps of damming loads based on configurations or debris type.

5. Correlation of debris damming loading

5.1 Linear Correlation with hydro-kinematics

In this section, the connection between hydro-kinematics and debris damming loads were analyzed by assessing how each peak debris damming loads correlate with flow variables. Here, flow depth (d), x-directional velocity (u), momentum flux (M), and Froude number (Fr) at the time of debris damming were used as the representative variable to characterize flow conditions. Specifically, the linear correlation between loads and flow variables was evaluated by quantifying the correlation coefficient, r, which is the ratio between the covariance of two variables and the product of their standard deviations (Snedecor and Cochran, 1980). In addition, the normalization for the peak damming loads was performed by dividing the measured peak damming loads by the maximum hydrodynamic loadings (non-debris case) that were listed in Table 4 about specific wave and configuration conditions. Similarly, for the flow variables, the values at the timestamp of a peak damming loading are divided by the maximum values of those variables in the non-debris case. In sum, all variables are normalized following $X^* = X_{peak}/\{X_0\}_{max}$. Where, X indicates a variable, such as $(F_{dam})_{FBP}$, $(F_{dam})_{LC}$, d, u, and M. X_{peak} is the value at peak damming loads in the structure or the central column, and corresponding flow variables at that time, and $\{X_0\}_{max}$ is the maximum variable in the non-debris case.

5.1.1 Effect of debris types

Fig. 17 compares the scatter maps of the normalized damming forces and corresponding flow variables (d^*, u^*, M^*, and Fr) at two different debris types, D1 (red circle) and D2 (blue circle) with a linear correlation. Here, Fig. 17a shows four scatter maps of each flow variable and normalized damming loadings on the structure, and Fig. 17b showed the matching correlation coefficient value (r) as a heatmap. Overall, a positive correlation (r > 0.5) was observed for all variables related to damming loads on the structure, with a stronger correlation seen at debris type D1 (red circle) than D2 (blue circle) across all variables. Specifically, the range of r is from 0.655 to 0.820 in D1, while it ranges from 0.519 to 0.678 in D2. The highest correlation was observed at the normalized momentum flux, M^*, for D1, and at the Froude number for D2. Notably, the correlation for M^* for D2 remains relatively high at 0.579, indicating a significant relationship between momentum flux and debris-induced loading overall.

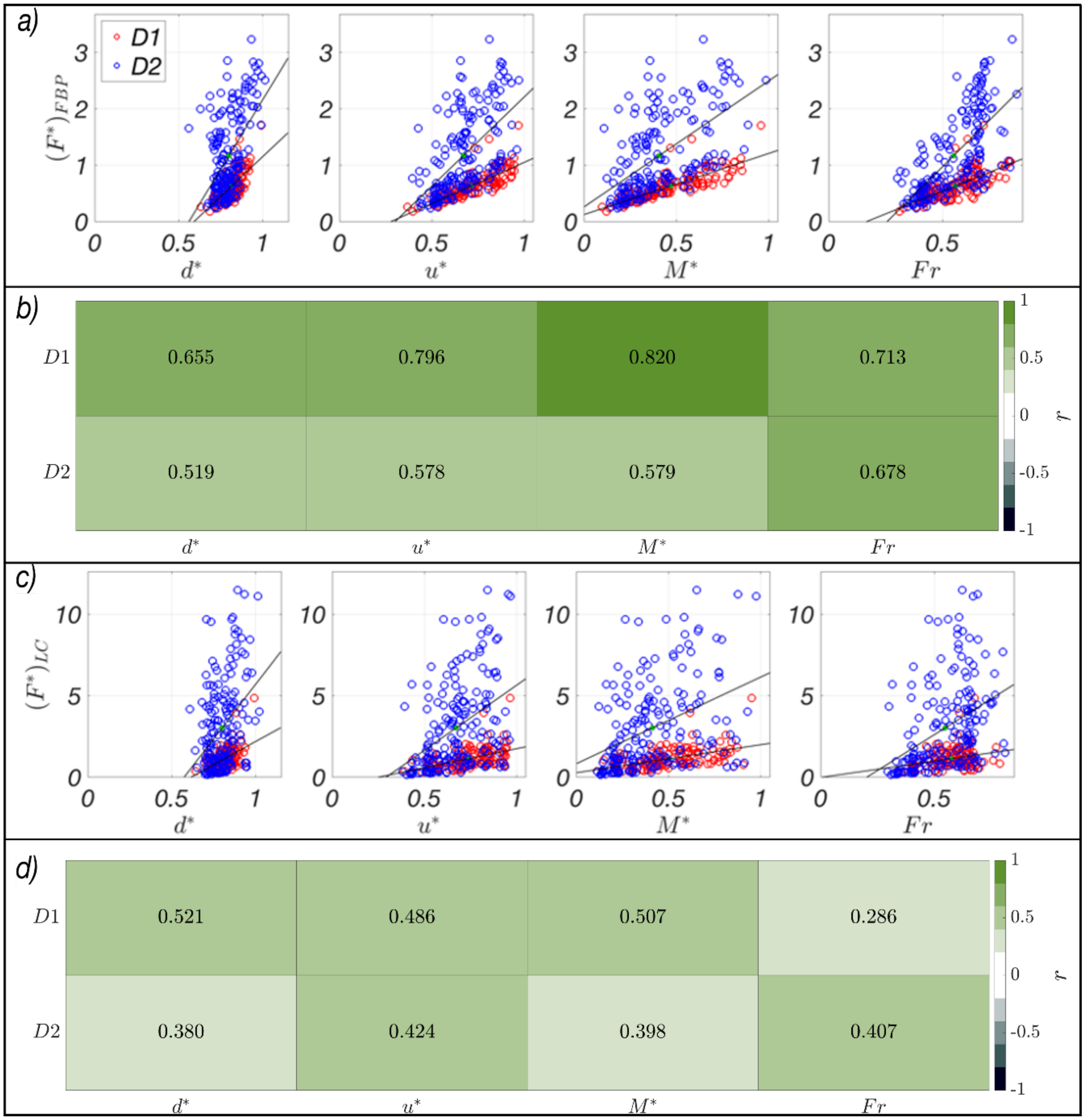

Fig 17. Scatter plots of normalized forces F^* to d^*, u^*, M^*, and Fr and Heatmap of correlation coefficients according to debris type.

Similarly, Fig. 17c and 17d depict scatter maps of flow variables and damming loads for the middle column and the heatmap of r values. As we had observed in Fig. 16, there were more uncertainties in the damming loads on the middle column than on the structure. Thus, the correlations on the middle column were generally lower compared to those observed on the structure, ranging from 0.380 to 0.521 for D1 and from 0.424 to 0.507 for D2. Despite being lower, these correlations still highlight the influence of normalized variables on debris-induced loading, with M^* exhibiting the strongest correlation among the variables considered.

It is also noteworthy that the value of normalized force was clearly dominated by the debris size. Mostly, smaller debris, D1 showed higher correlations with flow variables than D2 at the both structure and middle column. The maximum value of $(F^*)_{\mathrm{FBP}}$ at D1 is 1.7, while it is 3.2 at D2. Similarly, the maximum value of $(F^*)_{\mathrm{LC}}$ at D1 is about 5.0, while it is 11.0 at D2. These results indicate that larger damming loads are expected from larger debris at both the structure and the middle column. Additionally, we can observe the maximum value of normalized force at $(F^*)_{\mathrm{LC}}$ is significantly larger than the one at $(F^*)_{\mathrm{FBP}}$. This indicates that there may be much amplification of loading due to debris damming on a single column (component) rather than the whole structure.

5.1.2 Effect of structural configurations and flow conditions.

We noticed relatively lower correlations with D2 (12.2 m shipping container). In Figure 18, results are presented for each structural configurations and flow conditions (Conf. 1A, Conf. 1B, Conf. 2A, Conf. 3A) as scatter plots of the normalized damming forces at D2 versus normalized momentum flux, (M^*). We chose M^*as a representative flow variable because it showed the most correlation to damming forces in Fig. 17. Fig. 18a and b show the scatter map results on the structure and the middle column, while each Fig. 19c and 19d show corresponding correlation coefficient values in a heatmap format following the same structure as in Figs. 17. Conf. 1A and Conf. 1B indicate the same configuration and two different debris platforms (with debris platform and PVC cover plate).

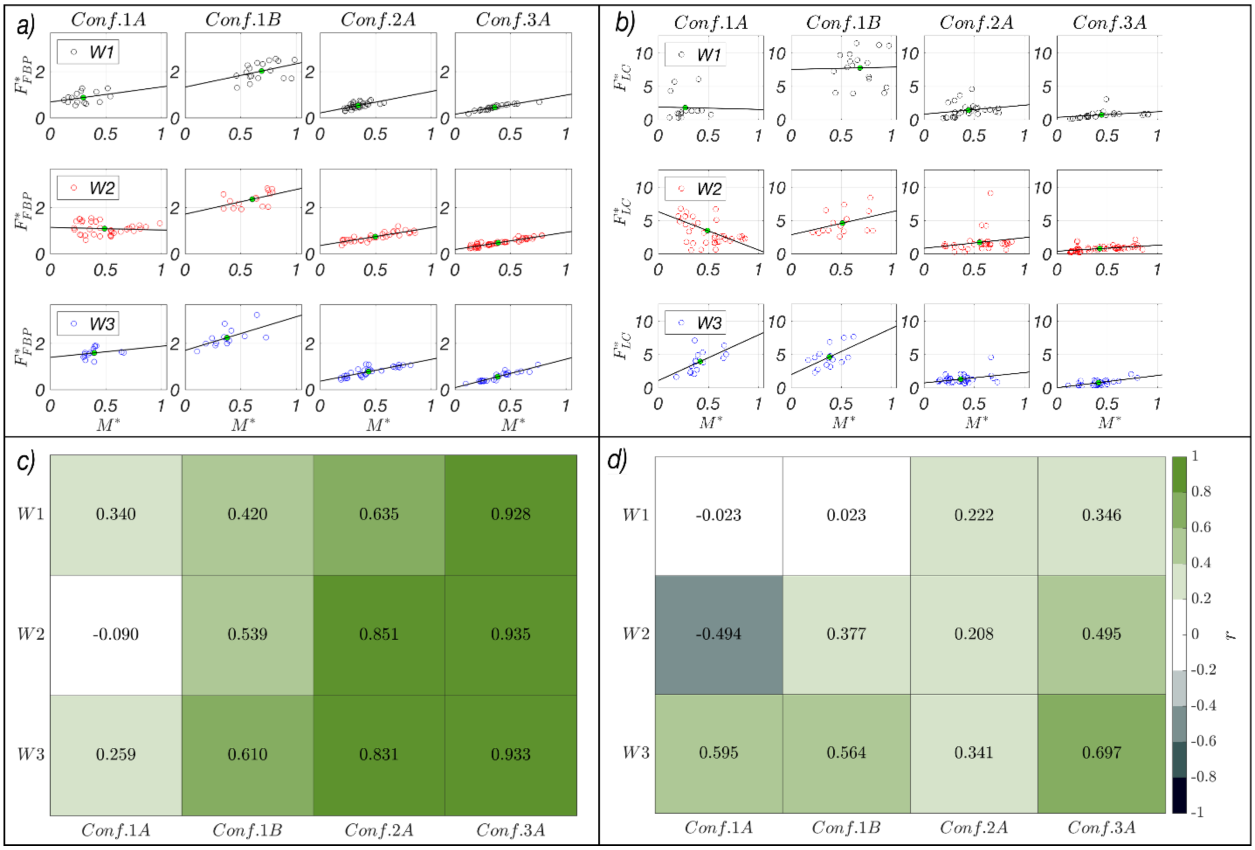

Fig 18. Correlations plots (a, b) and heat maps (c, d) of correlation coefficient between F^* and M^* according to the wave condition and configuration. Here, each color black, red, and blue indicates three different flow conditions (W1~W3).

In Fig. 18a and 18c, when we refined damming loads for each configuration and flow condition, one can observe a stronger correlation of $(F^*)_{\mathrm{FBP}}$ to M^* at Conf. 3A and ranges from 0.928 to 0.935. A relatively small but still significant correlation is found at Conf. 2A, ranging from 0.635 to 0.831.

A significant difference in patterns was observed between Conf. 1A and Conf. 1B across all flow conditions. Conf. 1B, utilizing the PVC plate and lower initial water depth, showed consistently higher and positive correlations ranging from 0.420 to 0.610. In contrast, Conf. 1A, utilizing the debris platform, exhibited relatively poor and sometimes negative correlations ranging from -0.090 to 0.340. During tests with the debris platform, mild hydraulic jumps and stronger turbulence were observed downstream of the platform, potentially introducing additional uncertainties in damming loads, unlike the tests with the PVC plate, where no hydraulic jump occurred. This sensitivity is particularly notable in determining damming patterns, especially in Conf. 1, which features a larger column space. Remarkably, correlations generally increased progressively from Conf. 1 to Conf. 3 within each flow condition. Notably, higher correlations were observed at W3 and W2 compared to W1.

In the case of $(F^*)_{\mathrm{LC}}$ in Fig. 18b and 18d, an increase in correlation can also be observed as the flow conditions change. Specifically, the range of correlation coefficient at Conf. 3 is 0.346 to 0.697, while a relatively smaller correlation was observed at Conf. 2 and Conf. 1. Similarly, poor correlation was found at Conf. 1A and better correlation at Conf. 1B, depending on the debris platform condition. Additionally, a clearer dependency on the correlation to wave condition can be observed here, with higher correlation found at W3 and smaller correlation at W2 and W1.

Negative correlations were observed at Conf.1A at W2 for both $(F^*)_{FBP}$ and $(F^*)_{LC}$. This trend is caused by the complex timing of debris dam formation and the number of debris dams. At W2 (Configuration 1A), we observed that a smaller number of debris pieces formed debris dams earlier, while a greater number of debris pieces formed debris dams at a relatively later time. This pattern resulted in an unexpected negative correlation only at W2.

Additional heatmap of correlation coefficients for other variables, such as d^*, u^*, and Fr with the same format as in Fig. 18c and 18d are available in the Appendix at Fig. A2.

5.2 Combined effect of parameters on the Damming Load

The above section investigated the individual effects of η^*, u^*, M^*, and Fr on the normalized debris damming loads based on categories of debris type (size), column configuration, and wave (flow) type. The results indicated there is a considerable amount of variation in the normalized loadings that cannot be explained by an individual variable. Therefore, as the next step, an n-way analysis of variance (Larson, 1992) was done to identify the combined effect of all the independent variables and their interactions on the normalized loads. Out of all the independent variables employed in this experiment, there are four continuous variables (η^*, u^*, M^*, and Fr) and three categorical variables (debris type, column configuration, and wave type). Therefore, the analysis of the combined effect of these independent variables needed an Analysis of covariance (ANCOVA) test which includes both categorical and continuous predictors. However, the dependent variable for the normalized forces failed to satisfy the normality and homogeneous variance assumptions for an ANCOVA test. Therefore, the analysis was continued with the PERmutational Multivariate ANalysis Of VAriance (PERMANOVA) test which is a semiparametric statistical test which is less sensitive to non-homogeneous variances (Anderson et al., 2017; Anderson and Walsh, 2013). Although PERMANOVA was originally used in the domain of multivariate analysis, it can also be used for univariate analysis. This analysis was performed using the *adonis2* function from the *vegan* package in *R* which considers Type I Sum of Squares (sequential SS) within the analysis. Furthermore, this function has the capability of handling both categorical and continuous variables together.

Since the sequential SS method was used in this analysis, the results of the PERMANOVA test depends on the order of the variables. Therefore, one-way analysis of variance tests was performed for each individual input variable. After that, the variables were sorted in the descending order of their importance based on the Type I SS. The order of variables presented in Tables 6 and 7 represents the sequence obtained from one-way analysis of variance of loading on the structure, and load on the middle column, respectively. In addition to the individual effects, the analysis focused on how the interactions between variables affect the variation in the normalized loads. Therefore, the PERMANOVA test considered the second-order interaction effects between the variables as well. The results of the PERMANOVA test for normalized loads on the structure and the single column are presented in Tables 6 and 7, respectively.

The continuous variables used in the variation analysis were tested for multicollinearity using Spearman's correlation coefficient matrix and variance inflation factor (VIF) (Fox and Weisberg, 2011). Momentum flux (M^*) was found to be highly correlated with the other continuous variables. However, momentum flux was still included in the PERMANOVA tests since it was the most influential variable on both normalized forces on the structure and middle column. Also, one of the main objectives is to determine the percentage of variation in damming forces that can be explained by the independent variables combinedly.

Table 6: Results of the n-way PERMANOVA test on the normalized forces on the structure.

	Degree of Freedom	Sum of Sqs	R^2	$Pr\ (>F^*)$
Wave type	5	9.23×10^{1}	7.26×10^{-1}	0.001
Column Conf.	2	1.74×10^{1}	1.36×10^{-1}	0.001
Fr	1	4.84×10^{0}	3.80×10^{-2}	0.001
M^*	1	8.16×10^{-3}	6.41×10^{-5}	0.565
u^*	1	2.18×10^{-1}	1.71×10^{-3}	0.004
η^*	1	3.14×10^{-1}	2.47×10^{-3}	0.004
Debris type	1	4.50×10^{-1}	3.54×10^{-3}	0.001
Wave type: Column Conf.	4	1.77×10^{0}	1.39×10^{-2}	0.001
Wave type: Fr	5	4.77×10^{-1}	3.75×10^{-3}	0.003
Wave type: M^*	5	4.50×10^{-1}	3.53×10^{-3}	0.002
Wave type: u^*	5	2.93×10^{-1}	2.30×10^{-3}	0.032
Wave type: η^*	5	4.49×10^{-1}	3.53×10^{-3}	0.004
Wave type: Debris type	3	9.18×10^{-1}	7.21×10^{-3}	0.001
Column Conf.: Fr	2	5.78×10^{-1}	4.54×10^{-3}	0.001
Column Conf.: u^*	2	1.43×10^{-1}	1.12×10^{-3}	0.046
u^*: η^*	1	1.64×10^{-1}	1.29×10^{-3}	0.011
Residual	255	6.20×10^{0}	4.87×10^{-2}	N/A
Total	314	1.27×10^2	1.00	N/A

Table 7: Results of the n-way PERMANOVA test on the normalized forces on the single column.

	Degree of Freedom	Sum of Sqs	R^2	$Pr\ (>F^*)$
Wave type	5	8.05×10^{2}	4.78×10^{-1}	0.001
Column conf.	2	2.44×10^{2}	1.45×10^{-1}	0.001
Debris type	1	5.80×10^{0}	3.44×10^{-3}	0.001
η^*	1	1.59×10^{1}	9.41×10^{-3}	0.565

Fr	1	6.04×10^{0}	3.59×10^{-3}	0.004
u^{*}	1	3.50×10^{0}	2.08×10^{-3}	0.004
M^{*}	1	5.65×10^{-1}	3.35×10^{-4}	0.001
Wave type: Column Conf.	4	2.40×10^{1}	1.43×10^{-2}	0.001
Wave type: Debris type	3	2.28×10^{1}	1.35×10^{-2}	0.003
Wave type: η^{*}	5	2.61×10^{1}	1.55×10^{-2}	0.002
Wave type: Fr	5	2.68×10^{1}	1.59×10^{-2}	0.032
Column Conf.: η^{*}	2	2.35×10^{1}	1.40×10^{-2}	0.004
Residual	254	4.26×10^{2}	2.53×10^{-1}	N/A
Total	313	1.68×10^{3}	1.00	N/A

The results of the one-way PERMANOVA tests for each single variable showed that all seven variables have a statistically significant effect on the normalized debris damming loadings. However, in the n-way analysis, some individual variables are observed to be statistically insignificant in relation to their effect on the normalized loadings. For example, in the n-way analysis for normalized forces on the structure, the effect of momentum flux, M^{*} is statistically insignificant. This happens since the Type I (Sequential) SS is considered in the n-way PERMANOVA test and due to multicollinearity between variables, the variation assigned to M^{*} in the one-way analysis is already accounted for by the three variables which are preceding M^{*} in the order of variables. Furthermore, the results of the interaction effects which are not within the level of significance 0.05 were removed from the original outputs of the PERMANOVA test when presenting Tables 6 and 7. However, it is important to note that every possible second-order interaction effect showed a statistically significant impact on the normalized loadings on both the structure and the middle column during one -way analysis.

As depicted by the results of the PERMANOVA test, wave type and column configuration account for the highest variations in the normalized debris damming loadings on the structure and the single column. However, the relative significance of debris type compared to other variables differs in the two models. Although debris type was the third most significant variable in the model for the single column loads, it was the least significant variable with the structure loadings. The lower rank of debris type in the structure normalized loading model, compared to the combined model of the single column, can be attributed to the high contribution of pure hydrodynamic forces to the loads on the structure. This reasoning was supported by having debris type as the third variable in the single column model where the contribution to the output loading was less. It further indicates that when debris damming loadings were dominating compared to pure hydrodynamic loads, the debris type had a significant effect on the loading acting on the middle column. When the effect of interactions between input variables was considered, almost similar interactions are observed to be significant in both models. However, the two interactions between wave type and u^{*} and M^{*} did not show a significant effect in the combined model for the single column, although these interactions were included in the model for the structure. This also can be possibly due to the less contribution pure hydrodynamic loads to the normalized forces of the single column.

As a measure of the ability of all variables to explain the variation in the normalized forces in a combined model, the R^2 values for the n-way PERMANOVA test were 0.94 and 0.74 for the structure and the single column, respectively. The R^2 value for the structure indicated that all the independent variables could combinedly account for nearly 95% of the variation in the normalized forces on the structure. On the other hand, it is noteworthy that only 75% of the variation was explained by the combined model for the normalized loads on the single column. It suggests that either more predictors are needed for explaining the remaining variation in the single column loadings or the remaining variation can be due to the high natural randomness associated with damming loadings, which meets our observations in Fig. 16 and Section 5.1.

6. Discussion

Considering the complexity of the tsunami-driven flow-debris-structure interactions including all debris impact and damming process in the fields, our experiment studies had to rely on test limits and several assumptions that can be further discussed.

We applied a transient wave to simulate specific characteristics of tsunamis, including their single, localized waveform and their ability to propagate over long distances without significant dispersion. The generated overland flows maintained mostly uniform Froude number ranged 0.5 and 0.7 at the test platform during the period of significant debris damming under the quasi-steady flow conditions. This Froude number is lower than the typical Froude number of 1.0 observed in the field. Therefore, we may expect a relatively larger F_{dam} / F_0 at higher Froude numbers, as we measured positive correlation between F_{dam} / F_0 and Froude number in Fig. 17.

Our observations indicated that the debris damming process reached a "saturation" point, where a maximum number of debris elements could be contained by the columns. Any additional debris arriving after this saturation point was reached were "deflected" by the hydrodynamic processes. Further analysis involving individual debris motion tracking, and the probability of impact and damming will be necessary to quantify these phenomena, although such advanced analysis is beyond the scope of the current study.

In addition, the ratio of F_{dam} / F_0 in our test showed relatively larger values than those found in previous damming studies (physical models) that used smaller amounts of debris. For example, the maximum F_{dam} / F_0 values for shipping containers debris, reported by Stolle et al. (2018) and Wuthrich et al. (2020) were 1.09 and 1.27 for shipping containers, while our test revealed ratios of 1.7 for D1 (6.1 meters shipping container) and 3.2 for D2 (12.2 meters shipping container). However, it's important to note that the duration of our tested wave is shorter compared to real-world tsunamis. Thus, longer-duration waves, such as dam-break waves are expected to exhibit higher damming loading at the time of maximum damming occurrence due to sustained wave energy throughout the event. Therefore, in future work, experimenting with waves of longer duration or incorporating additional factors such as dam-break waves or transient waves with a current will be recommended for more conservative results.

The scale of this study was set at 1:20 and presenting a whole structure rather than the part of the structure. This makes it the largest scale experiment compared to previous studies on damming loads (Stolle et al., 2018; Wüthrich et al., 2020). However, the actual size and number of columns in our study did not conform to exact structural design standards. The primary objective of this study was to elucidate the debris damming process and the resultant loads, rather than focusing on debris impact loading. For simplicity, we manufactured the debris as rigid bodies with uniform wood density. Since impact load is highly dependent on the stiffness of the debris itself, the measured quantification of the impact load in our study may not fully represent the actual impact load from prototype debris, such as shipping containers.

The direct correlation between flow variables and damming loads highlights the importance of considering hydrodynamic factors in structural design and risk assessment. Additionally, configuration adjustments, such as column spacing, were found to significantly impact damming occurrences and loading distribution. However, the current study only concentrated on two major homogeneous cases that represented shipping containers, disregarding the non-homogeneous nature of tsunami-induced debris observed in real-world scenarios. Consequently, in a forthcoming research endeavor, it is recommended to rectify this limitation by exploring non-homogeneous debris scenarios. This may involve incorporating a diverse range of debris shapes, sizes, and density.

7. Conclusion

Tsunami-driven debris damming phenomenon and consequent debris damming loading are investigated through 1:20 scale physical model studies. These experimental studies utilized 10 and 15 cuboid shaped debris as a group, representing an ideally scaled 12.2- and 6.1 meters shipping containers. Flow kinematics and loading conditions at the test structure that was composed of a number of different columns were measured under varied tsunamis-like wave conditions. A total of 228 test trials were performed accounting for two debris shapes, six wave conditions, and three structural configurations with different numbers of columns. The whole process of debris transport including debris entrainments, transports, collision, and damming were recorded by cameras and utilized to understand debris damming process and quantifying the time varying damming characteristics. The time series loadings data measured at the single column by the Loadcell (LC) and on the whole column structure by the Force Balance Plate (FBP) were resolved into impact and damming loading portions through low and high frequency filtering. Using the peak loading data, we quantified characteristics of debris damming loading under varied waves, debris size and configurations, and examined the correlation of the loadings to hydro-kinematics conditions.

The synthesis of the results provides the following conclusion that reveals the dynamics of debris-induced loading on a columns structure:

1) Compared to non-debris, the maximum peak damming loads increase about 3.2 times at the structure and 11.0 times at the single column. Additionally, the maximum damming loading was 3.4 times lower than the observed maximum impact loading at the whole column structure and 1.8 times lower than that observed at the single column.
2) Larger damming loadings were observed for larger debris (D2) and at higher intensity waves (W3) for the both structure and single column. However, relatively larger damming loads were observed at Conf. 3, the smallest spacing, for the structure, while at Conf. 1, the largest spacing, for the single column.
3) The narrowing of the spacing columns elevated the probability of damming occurrences, especially when debris size is smaller than the column spacing (e.g., D1 & Conf. 1), with only 17% of trials showing debris dams, compared to 91% for Conf. 2 and 100% for Conf. 3. However, consistent high probabilities of damming occurrence were observed regardless of the configurations when the debris size (e.g., D2) is larger than the column spacing.
4) Overall, distinctly higher correlations of debris damming loads to hydro-kinematic variables were observed at the structure than at the single column. Moreover, higher correlations were observed when column spacings are smaller than the debris, and relatively stronger correlations at a lower intensity wave (W1) compared to higher intensity wave (W3).
5) Normalized momentum flux (M^*) was observed to be the most influential variable affecting debris-induced damming loads, consistently exhibiting the strongest correlations across all categories. Additionally, u^*, d^* and Fr also demonstrated notable correlations, further highlighting their role in predicting debris-induced damming loads.
6) The n-way PERMANOVA results show that independent variables collectively explain about 95% of the variation in normalized loadings on the structure; while for the single column, only 75% of the variation is accounted for. This indicates either the need for more predictors to explain the remaining variation, or it could be attributed to the high natural randomness associated with damming forces on the column.

Overall, our findings provide valuable insights into the complex interplay between debris characteristics, structural configurations, and hydrodynamic variables in influencing debris-induced loading on coastal structures. By elucidating the relationships between these factors, our study contributes to the advancement of coastal engineering practices aimed at enhancing the resilience of coastal structures against debris-induced hazards. Further research in this area is warranted to refine our understanding and develop effective strategies for mitigating the risks associated with debris-induced load.

Acknowledgment

This material is based upon work supported by the National Science Foundation Division of Civil, Mechanical, and Manufacturing Innovation (CMMI) and Natural Hazards Engineering Research Infrastructure (NHERI) through Grants #2203131, #2203116 and #2037914. The content expressed in this paper and the authors' view does not necessarily represent the views of the National Science Foundation. The authors would like to thank Tim Maddux and Rebekah Miller at the Hinsdale Wave Research Laboratory for their assistance in the experiment setup.

References

Alcala, E. R. D., Voerman, J. A., Konrath, J. M., & Vydhyanathan, A. Xsens DOT Wearable Sensor Platform White Paper.

Applied Technology Council, National Earthquake Hazards Reduction Program (US) and National Tsunami Hazard Mitigation Program (US), (2008). Guidelines for design of structures for vertical evacuation from tsunamis. US Department of Homeland Security, Federal Emergency Management Agency.

Arikawa, T., Ohtsubo, D., Nakano, F., Shimosako, K. and Ishikawa, N. (2007). Large model tests of drifting container impact force due to surge front tsunami. In Proceedings of coastal engineering, JSCE (Vol. 54, pp. 846-850). Japan Society of Civil Engineers.

ASCE/SEI (2016) "Minimum design loads for buildings and other structures." ASCE/SEI 7-16, Reston, VA.

ASCE/SEI (2022) "Minimum design loads for buildings and other structures." ASCE/SEI 7-22, Reston, VA.

Bocchiola, D., Rulli, M. C., & Rosso, R. (2008). A flume experiment on the formation of wood jams in rivers. Water Resources Research, 44(2).

Chock, G. Y. (2016). Design for tsunami loads and effects in the ASCE 7-16 standard. Journal of Structural Engineering, 142(11), 04016093.

Fox, J. and Weisberg, S. (2018). An R companion to applied regression. Sage publications.

Ghobarah, A., Saatcioglu, M. and Nistor, I. (2006). The impact of the 26 December 2004 earthquake and tsunami on structures and infrastructure. Engineering structures, 28(2), pp.312-326.

Kameshwar, S., Park, H., Cox, D.T. and Barbosa, A.R. (2021). Effect of disaster debris, floodwater pooling duration, and bridge damage on immediate post-tsunami connectivity. International journal of disaster risk reduction, 56, p.102119.

Ko, H.S., Cox, D.T., Riggs, H.R. and Naito, C.J. (2015). Hydraulic experiments on impact forces from tsunami-driven debris. Journal of Waterway, Port, Coastal, and Ocean Engineering, 141(3), pp.04014043.

Larson, D.A., 1992. Analysis of variance with just summary statistics as input. The American Statistician, 46(2), pp.151-152.

Naito, C., Cercone, C., Riggs, H.R. and Cox, D. (2014). Procedure for site assessment of the potential for tsunami debris impact. Journal of Waterway, Port, Coastal, and Ocean Engineering, 140(2), pp.223-232.

Nistor, I., Goseberg, N. and Stolle, J. (2017). Tsunami-driven debris motion and loads: A critical review. Frontiers in Built Environment, 3, p.2.

Oudenbroek, K., Naderi, N., Bricker, J. D., Yang, Y., Van der Veen, C., Uijttewaal, W., ... & Jonkman, S. N. (2018). Hydrodynamic and debris-damming failure of bridge decks and piers in steady flow. Geosciences, 8(11), 409.

Park, H., Cox, D. T., Lynett, P. J., Wiebe, D. M., and Shin, S. (2013). Tsunami inundation modeling in constructed environments: A physical and numerical comparison of free-surface elevation, velocity, and momentum flux. Coastal Engineering, 79, 9-21.

Park, H., Koh, M.J., Cox, D.T., Alam, M.S. and Shin, S. (2021). Experimental study of debris transport driven by a tsunami-like wave: Application for non-uniform density groups and obstacles. Coastal Engineering, 166, p.103867.

Reese, S., Cousins, W.J., Power, W.L., Palmer, N.G., Tejakusuma, I.G. and Nugrahadi, S. (2007). Tsunami vulnerability of buildings and people in South Java–field observations after the July 2006 Java tsunami. Natural Hazards and Earth System Sciences, 7(5), pp.573-589.

Schmocker, L., & Hager, W. H. (2011). Probability of drift blockage at bridge decks. Journal of Hydraulic Engineering, 137(4), 470-479.

Schmocker, L., & Hager, W. H. (2013). Scale modeling of wooden debris accumulation at a debris rack. Journal of Hydraulic Engineering, 139(8), 827-836.

Shekhar, K., Winter, A. O., Alam, M. S., Arduino, P., Miller, G. R., Motley, M. R., ... & Cox, D. T. (2020). Conceptual evaluation of tsunami debris field damming and impact forces. Journal of Waterway, Port, Coastal, and Ocean Engineering, 146(6), 04020039.

Shekhar, K., Winter, A.O., Alam, M.S., Arduino, P., Miller, G.R., Motley, M.R., Eberhard, M.O., Barbosa, A.R., Lomonaco, P. and Cox, D.T. (2020). Conceptual evaluation of tsunami debris field damming and impact forces. Journal of Waterway, Port, Coastal, and Ocean Engineering, 146(6), p.04020039.

Shultz, J. (2022). Application of Motion Capture Technologies to Assess the Free Surface and Track Waterborne Debris in Wave Research Laboratories, Oregon State University, Master thesis.

Snedecor, G. W. and Cochran, W. G. Statistical Methods, 7th ed. Ames, IA: Iowa State Press, p. 180, 1980.

Stolle, J., Takabatake, T., Mikami, T., Shibayama, T., Goseberg, N., Nistor, I. and Petriu, E. (2017). Experimental investigation of debris-induced loading in tsunami-like flood events. Geosciences, 7(3), p.74.

Stolle, J., Takabatake, T., Nistor, I., Mikami, T., Nishizaki, S., Hamano, G., Ishii, H., Shibayama, T., Goseberg, N. and Petriu, E. (2018). Experimental investigation of debris damming loads under transient supercritical flow conditions. Coastal Engineering, 139, pp.16-31.

Takahashi, S., Sugano, T., Tomita, T., Arikawa, T., Tatsumi, D., Kashima, H., Murata, S., Matsuoka, Y. and Nakamura, T. (2010). Joint survey for 2010 Chilean earthquake and tsunami disaster in ports and coasts. Port and Airport Res Inst.

Wüthrich, D., Ylla Arbós, C., Pfister, M. and Schleiss, A.J. (2020). Effect of debris damming on wave-induced hydrodynamic loads against free-standing buildings with openings. Journal of Waterway, Port, Coastal, and Ocean Engineering, 146(1), p.04019036.

Yeh, H., Barbosa, A.R., Ko, H. and Cawley, J.G. (2014). Tsunami loadings on structures: Review and analysis. Coastal Engineering Proceedings, 1(34), p.4.

Appendix.

Fig. A1 The other two wave conditions used in this test.

Each Fig. A1 (a) and (b) provides time-series of surface elevation (η) at wave gauges for W1A and W3A conditions following the format of Fig. 7. In similar manner, each Fig. A1 (c) and (d) shows x-directional velocity, u at three velocimeters for W1A and W3A.

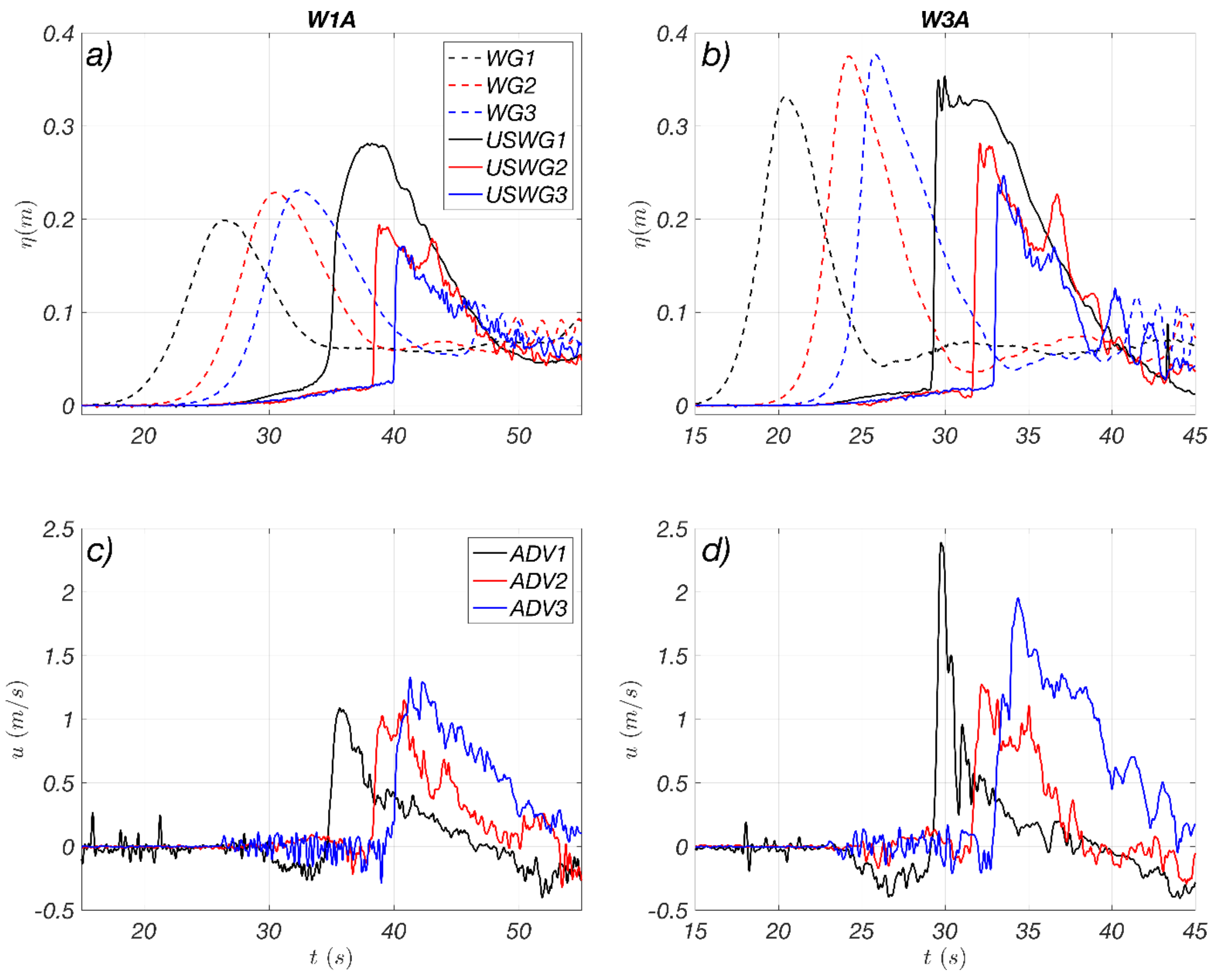

Fig. A1. Time series of surface elevation at wave gauges at W1A and Conf (a). and at W3A, and Conf. 3 (b). The x-velocities for non-debris conditions at W1A and Conf. 3 (c), and at W3A and Conf. 3 (d).

Fig. A2 Correlations heatmap of correlation coefficients for other variables.

Fig. A2 shows the heatmap of the linear correlation coefficient values for d^* and Fr with the same format as in Fig. 18b and 18d. In the case of the structure, it can be clearly observed that the configuration of the structure had the most significant effect on the correlation, with different configurations resulting in varying levels of correlation at different flow conditions. Specifically, for d^*, the values of correlation coefficients consistently increased from Conf. 1 to Conf. 3 across all flow conditions, which followed the same pattern as in Fig. 18. This observation indicates that the arrangement and spacing of the columns in the structure had a notable impact on the damming load patterns experienced by the structure.

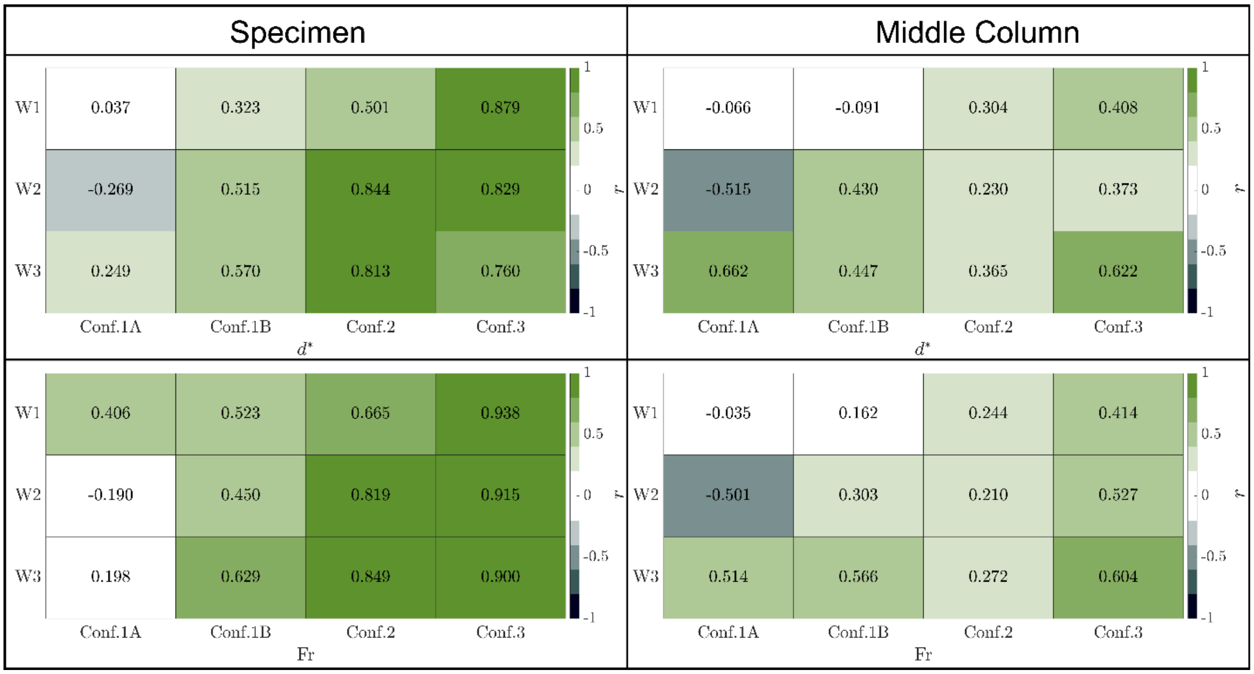

Fig A2. Correlations heatmap of correlation coefficient for d^* (top panel) and Fr (bottom panel) according to the wave condition and configuration.